Astronomy & Astrophysics manuscript no. output
November 11, 2026
©ESO 2026

Euclid Data Release 1 (DR1)

Near-infrared processing and data products

Euclid Collaboration: G. Polenta, M. Frailis, A. Alavi, P. N. Appleton, P. Awad, A. Bonchi, L. Bramante, G. Calderone, et al.

(Full author list and affiliations details can be found after the references)

ABSTRACT

The *Euclid* near-infrared processing function (NIR PF) converts the raw observations acquired by the Near-Infrared Spectrometer and Photometer (NISP) into calibrated images and source-level products. Following the first implementation delivered with the Euclid Quick Data Release 1 (Q1), the NIR PF has been revised for the first major Euclid Data Release (DR1), with improvements to detector-level processing, calibration, image reconstruction, and quality control. The DR1 processing includes observations covering more than 1900 deg^2 and has produced 71 659 calibrated near-infrared (NIR) images. We assess the performance of the processing chain through extensive astrometric and photometric validation. The astrometric solution reaches an average root-mean-square (RMS) of 10 mas, remaining below 20 mas for 99% of the dithers in all three NISP bands. Temporal variations in the instrumental throughput are typically corrected to a level of 2 mmag RMS, while the relative photometric accuracy reaches 0.9% for sources brighter than 19 mag in Y_E, J_E, and H_E, and the residual spatial variations of the photometric calibration across the focal plane are at the level of approximately 10 mmag for the entire sample. Despite some remaining limitations, the DR1 NIR imaging products are consistent with the required astrometric and photometric performance over the large area covered by this release.

Key words. Cosmology: observations – Surveys – Techniques: image processing – Techniques: photometric – Space vehicles: instruments – Instrumentation: detectors

1. Introduction

The ESA *Euclid* space mission, launched on 1 July 2023, is conducting a wide and deep survey of the extragalactic sky to investigate the nature of dark matter and dark energy and the evolution of the large-scale structure of the Universe (Euclid Collaboration: Mellier et al. 2025). *Euclid* is equipped with two complementary instruments: the visible imager (VIS, Euclid Collaboration: Cropper et al. 2025); and the Near-Infrared Spectrometer and Photometer (NISP, Euclid Collaboration: Jahnke et al. 2025), which provides both near-infrared imaging and slitless spectroscopy. The NISP photometric channel covers the wavelength range from 950–2021 nm through the three broadband filters Y_E, J_E, and H_E (Euclid Collaboration: Schirmer et al. 2022), using 16 HAWAII-2RG (H2RG) near-infrared detectors of 2048×2048 pixels each, with a pixel scale of $0''.3$ and a field of view of 0.57 deg^2.

The NIR PF is the Euclid Science Ground Segment (SGS) block (Euclid Collaboration: Ruffenach et al. 2026) responsible for transforming the raw NISP photometric observations into calibrated imaging products through a sequence of detector-level corrections, calibration, and image-processing steps, ultimately producing calibrated images and associated source-level products. The first implementation of the NIR PF was described in the context of the Euclid Quick Data Release 1 (Q1; Euclid Collaboration: Polenta et al. 2026, hereafter NIRQ1), which provided NISP imaging over 63.1 deg^2 and served as the first large-scale validation of the processing chain. Building on this experience, the NIR PF has been revised and extended for the first major Euclid Data Release (DR1; Euclid Data Release 1 2026; Euclid Collaboration: Aussel et al. 2026). The DR1 processing includes observations acquired between 1 October 2023 and 21 May 2025, covering a total area of more than 1900 deg^2 across the Euclid Wide Survey (EWS) and the Euclid Deep Survey (EDS), as well as the COSMOS field and dedicated calibration fields (Euclid Collaboration: Scaramella et al. 2022; Euclid Collaboration: Tereno et al. 2026). In total, the DR1 processing produced 71 659 calibrated NIR images.

This paper presents the DR1 implementation of the NIR PF, describing its updated processing algorithms, calibration strategy, data products, and validation on the first year of *Euclid* survey observations. Specific aspects of the NIR data processing and characterisation are presented in dedicated companion papers, focusing on the astrometric calibration in Euclid Collaboration: Radovich et al. (2026), the point-spread function (PSF) in Euclid Collaboration: da Silva et al. (2026), and persistence effects in Euclid Collaboration: Kubik et al. (2026).

2. In-flight stability of the NISP Instrument

Overall, NISP has been operating very consistently since launch, with no major evolution of instrumental properties except the slow buildup of water ice on NISP's detector surfaces (Euclid Collaboration: Schirmer et al. 2023). The physical number of unusable 'bad' pixels has not changed significantly since launch, although their characterisation and flagging has been updated (see Sect. 3.1.1, and compare Table A.1 for DR1 with table 1 in NIRQ1 for Q1). The characterisation of charge persistence continues to be improved (Sect. 3.1.3 here, and Euclid Collaboration: Kubik et al. 2026), but the overall persistence properties of the detectors as a function of short- and long-term illumination do not seem to evolve. Similarly, focal plane geometry (relative positions and orientations of the detectors) derived from astrometric calibration is consistent with pre-launch metrology, thus

indicating that the instrument itself is absolutely stable in this respect.

Remarkably, since launch and through Solar maximum, the flux of the light-emitting diodes (LEDs) in NISP's calibration lamp (NI-CU, Euclid Collaboration: Hormuth et al. 2025) have been stable to within 0.1% at a given driver current. This order of stability was guaranteed for periods of 1200 s only. Since the LEDs illuminate the detectors directly without intervening optics, this stability allows accurate long-term monitoring of detector characteristics, such as the build-up of ice the detector surfaces (Sect. 3.2.1). Using empirical coating models, the estimated contamination rate of $\sim 10\,\mathrm{nm\,month^{-1}}$ is consistent with pre-launch expectations (Euclid Collaboration: Schirmer et al. 2023, 2026b). Due to interference, the effective quantum efficiency (QE) is variable as a function of time and wavelength (sect. 7.7 in Euclid Collaboration: Schirmer et al. 2026a). For DR1, the differential evolution between LEDs of different wavelengths was still limited, compensated on a per-band basis by relative flux calibration (Sect. 4.2 here, and section 3.2.2. of NIRQ1). In future data releases, these contamination effects will be accounted for using time-dependent corrections of the QE curves.

3. The NIR processing function

A detailed description of the NIR PF is presented in NIRQ1 in the context of the Q1 data release. Here, we focus on the main changes and improvements introduced in the current DR1 version with respect to this initial implementation.

3.1. Common NIR–SIR pre-processing

3.1.1. Bad-pixel identification and masking

In the master bad-pixel mask (BPM), 'disconnected' pixels (see section 3.1.3. of NIRQ1 for a description of bad pixel flavours) were updated using the performance verification (PV) flat-fields (PV-010, Euclid Collaboration: Schirmer et al. 2026a) taken with `LedId=B`, `Intensity=60`, and `PwmDutyCycle=28.7`. 'Hot' pixels were updated using 500 PV photo darks (PV-012, Euclid Collaboration: Schirmer et al. 2026a).

Permanently 'saturated' pixels were missing and are now included in the BPM, flagged as `INVALID`. Saturated pixels are identified across a set of dark current frames. The method involves a running pair-wise comparison of the frames. For each pair, the pixels that are simultaneously saturated in both frames are identified, and their number is recorded. The pair yielding the minimum number of commonly saturated pixels is then selected, and the corresponding pixel population is taken as an estimate of the permanently saturated pixels. The saturation limit is defined as a threshold close to the A/D conversion limit, accounting for both readout and numerical noise.

Another new category in the BPM are pixels forming cross-shaped 'flower' patterns, where the central pixel misses the indium interconnect between the HgCdTe detector layer and the readout integrated circuit. The charge in this pixel is largely lost, rendering it dark ('flower centre'), while some signal leaks into its adjacent pixels, which then appear brighter than normal ('flower petals'). These types of defect are known as 'open' and 'adjacent to open' pixels in the *James Webb* Space Telescope (JWST) data (Rauscher et al. 2014). We identify them using a Laplace filter on a sequence of 30 LED flat-field exposures. A central pixel must be identified in at least two exposures, and is then flagged as `FLOWER` and `INVALID`, together with the four adjacent pixels.

The BPM is not restricted to scientifically inoperable pixels. To distinguish unusable from informational flavours, the bit 0 – 'INVALID' – is reserved for the unusable cases. Statistics for the non-transient – that is static – bad-pixel types are summarised in Table A.1. Overall, we identified a total of 239 878 `INVALID` bad pixels corresponding to approximately 0.4% of the focal plane. Per detector, we find between 5177 and 31 700 bad pixels, with a mean of 14 992.

3.1.2. Non-linearity correction

The non-linearity correction follows the procedure described in Q1 (NIRQ1), where the per-pixel response is modelled as a 4th-degree polynomial mapping the measured non-linear flux to a linearised estimate, calibrated against LED flat-field exposures at multiple flux levels. For DR1, the calibration coefficients have been updated using in-flight data from two calibration campaigns: PV-018 (November 2023) and F-008 (February–October 2024), comprising 2136 exposures taken in MACC(4,16,4) mode across six flux levels spanning 8 to $750\,\mathrm{e^-\,s^{-1}}$ (Euclid Collaboration: Schirmer et al. 2026a). The highest flux setting ($951\,\mathrm{e^-\,s^{-1}}$) was excluded due to frequent outliers in the final ramp group induced by saturation. The new DR1 non-linearity coefficients are in good agreement with the ground measurements used for Q1, confirming detector stability through launch and commissioning. The validity range of the correction and the treatment of out-of-range pixels remain unchanged; extension to a wider dynamic range is planned for Euclid Data Release 2 (DR2).

3.1.3. Persistence masking

In Q1 processing (NIRQ1), the persistence model was derived from ground-characterisation data. This model included only the fast-decay component over short timescales, but the non-linear dependence of the persistence amplitude and decay index (defined below) on the previous illumination intensity was taken into account. Persistence was considered only from spectroscopic to photometric exposures within the same dither (15-minute history), while persistence in spectroscopic exposures from preceding photometric exposures was not allowed for.

The pipeline was refactored for DR1, and the persistence model updated using in-flight calibration data (Euclid Collaboration: Kubik et al. 2026). The adopted model is based on the decay of persistence following a $60\,\mathrm{ke^-}$ illumination in the PV-016 calibration data set (Euclid Collaboration: Schirmer et al. 2026a), parameterised as

$$I_\mathrm{P}(S,t) = \tilde{\alpha} S\,(t-\tilde{t}_0)^{-\tilde{\beta}}\,, \tag{1}$$

where $\tilde{\alpha}$ and $\tilde{\beta}$ denote the initial persistence current amplitude and the decay index, respectively, after a signal S, and $\tilde{t}_0$ is the midpoint of the source exposure. The dependence of $\tilde{\alpha}$ and $\tilde{\beta}$ on the prior illumination intensity is neglected.

Creation of the persistence image A persistence image is computed using a dedicated pipeline for every science – or target – exposure, by summing the time-integrated power-law decays from the N preceding exposures,

$$P(S,t,t_\mathrm{int}) = \sum_{i=1}^{N} \frac{\tilde{\alpha} S_i}{1-\tilde{\beta}} \left[(t_i + t_\mathrm{int})^{1-\tilde{\beta}} - t_i^{1-\tilde{\beta}} \right]. \tag{2}$$

Here, $t_{\rm int}$ is the integration time of the target exposure, S_i the signal in the i-th preceding exposure, and t_i the time between the midpoints of that preceding exposure and the target exposure.

The working principles are as follows: (i) following a saturation event, a pixel is masked for the full look-back time of 5 h, as its true signal and therefore persistence are unknown; (ii) persistence contributed by different exposures is approximately additive, a simplification that facilitated pipeline implementation (Kubik et al. 2024; Euclid Collaboration: Kubik et al. 2026); (iii) the computation is signal-driven, that is persistence from photo-ionisation and particle ionisation is assumed to behave identical, despite the true amount of charge generated by a particle is masked by the on-board slope fit; (iv) the sky background is ignored, as its persistence signal is assumed to be negligible and mostly removed with background subtraction.

For DR1 processing, the temporal window for persistence computation was set to 5 hours for both photometric and spectroscopic targets. In terms of exposure selection, both photometric and spectroscopic exposures were included when constructing persistence images for spectroscopic targets, while only spectroscopic exposures were considered for photometric targets.

Application of the persistence mask The application step uses persistence images produced by the pipeline to identify and flag persistence contamination in science exposures. For each target and its corresponding persistence image, the persistence signal is evaluated pixel by pixel. Pixels exceeding the relevant threshold are flagged with the `PERSIST` and `INVALID` flags in the DQ layer. For photometric targets a threshold of $2\,e^-$ is used following the current requirements (sect. 5.2 in Euclid Collaboration: Kubik et al. 2026), while for spectroscopic data, the masking threshold of $30\,e^-$ was optimised using purity and completeness of spectrometric redshifts (Euclid Collaboration: Le Brun et al. 2026). The threshold is applied independently of the intensity of the signal in the target exposure for both photometric and spectroscopic targets. The `PERMODFAIL` flag is raised for pixels where the persistence estimate may be unreliable, for example, if a pixel in the history exposures is saturated or affected by cosmic rays and energetic particle hits, or if the persistence model coefficients are undefined. The science exposure header is updated with the threshold values used, along with summary statistics per detector, including the number of masked, corrected, failed, and invalid pixels.

For photometric targets, an Hough transform (HT; Hough 1962) line detection is applied to the target exposure to enhance masking of persistence streaks. Pixels belonging to detected linear features are flagged with `PERSIST` in the DQ layer if they have not already been flagged via thresholding of the persistence image. For the implementation on *Euclid* images, a threshold is first applied on the image, and the positions of surviving pixels are used for the calculation. To avoid flagging diffraction spikes, which remain attached to their stars after thresholding, connected components larger than 10 000 pixels are removed prior to the HT, while a minimum line length of 200 pixels excludes the shorter spikes of fainter stars. The probabilistic version of the HT has been used here, specifically `scikit-image`'s `probabilistic_hough_line` function, since this is the version of the method that is capable of returning the end points of the detected lines in addition to their location and orientation, and is moreover much less computationally expensive. When applied within the NIR PF as a step following the power-law masking, the HT offers a geometric approach to search for any residual linear structures in the images that remained undetected. This contributes an additional 2% of the number of pixels flagged by the power-law model, which is an indication that the latter is successful in masking the vast majority of persistence traces in the images, leaving few remainders for the HT to detect.

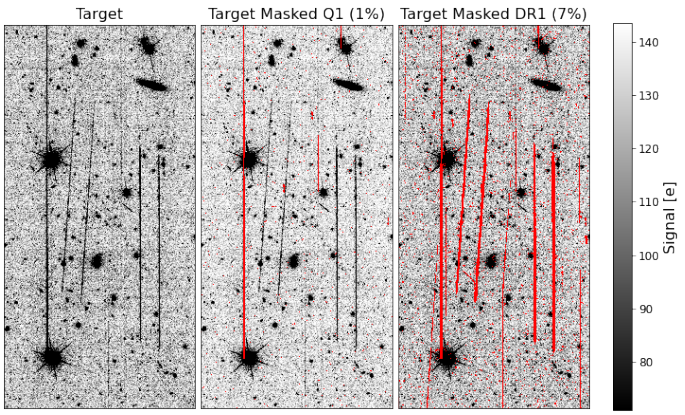


Fig. 1. Comparison of persistence masking in Q1 and DR1 in a 500×1000-pixel region. Masked pixels are shown in red. Persistence from some spectra is unmasked in Q1 but masked in DR1 due to the longer history considered when computing the persistence image. The fraction of masked pixels is indicated in parentheses above each panel.

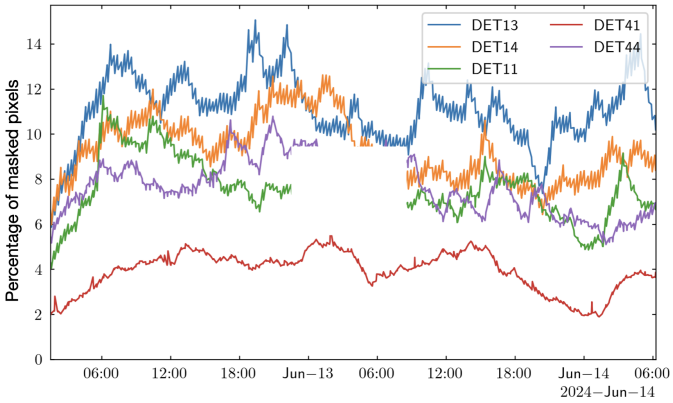


Fig. 2. Fraction of masked pixels in DR1 processing for the five detectors with the highest persistence in SkyPatch 38 during a period of high solar activity. For some detectors, the masking fraction exceeds 10% due to the high flux of energetic particles and limitations of the persistence model.

Persistence masking: Q1 versus DR1 Figure 1 highlights the improvement in persistence masking in DR1 with respect to Q1 processing. Persistence from some spectra is unmasked in Q1, but correctly masked in DR1, due to the longer illumination history considered in the pipeline. However, DR1 processing sometimes masks too many pixels because the masking parameters are very conservative (Euclid Collaboration: Kubik et al. 2026). Figure 2 shows the fraction of pixels masked in DR1 processing for SkyPatch 38, consisting of 43 observations in the EDF-North (Euclid Collaboration: Scaramella et al. 2022) acquired during a period of high solar activity. Several detectors exhibit masking above 10%. This is partly caused by the enhanced flux of energetic particles during high solar activity, and partly by limitations of the persistence model, which does not fully account for dependencies on signal intensity, nor the different behaviour of persistence generated by photo- and particle ionisation.

While the model presented in Euclid Collaboration: Kubik et al. (2026) and adopted in this work successfully identifies and masks pixels affected by persistence, accurately predicting the associated excess flux remains challenging. Consequently, a further increase in the number of usable pixels may be achieved by applying persistence corrections rather than relying on masking alone. Several alternative correction approaches are currently being investigated to improve the accuracy of the correction and assess their suitability for potential inclusion in the Euclid DR2 processing pipeline and subsequent data releases. A comprehensive comparison of these approaches will be presented in Awad et al. (in prep.).

3.2. Astrometric and photometric calibration of NISP images

3.2.1. Pixel-response non-uniformity (PRNU) correction

The Euclid DR1 processing corrects PRNU in all three bands using filter-dependent master flats derived from LED exposures, following NIRQ1. Each of the five LEDs, designated A to E, in the NI-CU produces a near-monochromatic spectral energy distribution (SED) and illuminates the focal-plane array (FPA) directly at a small off-axis angle, without passing through a filter (Euclid Collaboration: Hormuth et al. 2025). The LEDs B, C, and D provide the exposures used to derive the $Y_{\rm E}$, $J_{\rm E}$, and $H_{\rm E}$ master flats, respectively. For each LED, we calibrate 30 exposures using the pre-processing steps in Sect. 3.1 and combine them into a master flat. Section 3.2.1 and appendix A of NIRQ1 describe the conversion from calibrated LED flats to filter-dependent master flats using the QE map and filter transmission curve.

We used one set of filter-dependent master flats throughout DR1 processing. To assess temporal changes, we examined 24 $H_{\rm E}$ master flats constructed from LED-D exposures between March 2024 and April 2026. This monitoring sequence covers part of the DR1 observing period and extends beyond it.

We denote the master flat for detector d at epoch t and pixel $\mathbf{x}$ by $\mathcal{F}_d(\mathbf{x}, t)$, and use the same set of valid pixels, Ω_d, at every epoch. We isolate the small-scale component $S_d(\mathbf{x}, t)$ as

$$S_d(\mathbf{x}, t) = \frac{\mathcal{F}_d(\mathbf{x}, t)}{G_\sigma[\mathcal{F}_d(\mathbf{x}, t)]}\,, \tag{3}$$

where G_σ is a mask-aware Gaussian smoothing operator with standard deviation $\sigma = 64$ pixels. This procedure effectively suppresses large-scale variations while preserving local pixel-to-pixel fluctuations. For a fixed mask, a detector-wide multiplicative normalisation cancels between the numerator and denominator. Mask construction and smoothing checks are described in Appendix B.1.

We characterise spatial variability using

$$\sigma_{68}(S) = \frac{P_{84}(S) - P_{16}(S)}{2}\,, \tag{4}$$

where P_p is the pth percentile over valid pixels. The median static PRNU amplitude, $\sigma_{68}(S_d)$, across the 16 detectors changes from 1.269% at the first epoch to 1.272% at the final epoch. The change is 0.0029 percentage points, or 0.23% of the initial amplitude. This statistic measures the spatial structure within each master flat; its stability does not imply that every pixel remains unchanged.

We measure temporal variability using the logarithmic residual

$$\Delta \ln S_d(\mathbf{x}; t_i, t_j) = \ln\left[\frac{S_d(\mathbf{x}, t_j)}{S_d(\mathbf{x}, t_i)}\right]\,. \tag{5}$$

For small changes, this residual approximates the fractional change in the small-scale component; percentages below denote $100\,\Delta \ln S_d$. The early reference, $S_{d,\rm early}$, is the pixel-wise median of the first three epochs. We compare subsequent epochs with this reference and consecutive epochs with one another.

To test whether the residuals grow with temporal separation without selecting a fixed reference, we calculate a robust temporal structure function (SF) as

$$\mathrm{SF}(\tau) = \frac{1}{\sqrt{2}}\,\mathrm{median}_{(d,i,j)\in\mathcal{P}_\tau}\,[\sigma_{68}(\Delta \ln S_d)]\,, \tag{6}$$

where $\mathcal{P}_\tau$ contains all detectors and distinct epoch pairs with $i < j$ and $t_j - t_i$ in lag bin τ. We first calculate σ_{68} over the valid pixels of each detector and then take the median over detector–pair measurements. The $1/\sqrt{2}$ factor gives a single-epoch-equivalent amplitude for independent, approximately Gaussian fluctuations of comparable amplitude.

At the final epoch, the median reference-relative scatter across detectors is 0.326%, with a range of 0.309–0.347% (Fig. 3a). Across adjacent-epoch comparisons of all detectors, the median scatter is 0.359%, with 16th–84th percentiles of 0.356–0.364%; no focal-plane-wide discontinuity is seen (Fig. 3b). The structure function rises from $0.2541\% \pm 0.0002\%$ below 90 days to $0.2652\% \pm 0.0012\%$ at 550–800 days (Fig. 3c). These uncertainties are leave-one-epoch-out jackknife standard errors. The rise remains positive when any epoch is omitted. The short-lag value is consistent with $0.359\%/\sqrt{2}$; the higher long-lag value indicates a time-dependent contribution to the differences between delivered master flats, although without identifying its origin.

We also compare pixel-wise median stacks of the final three and first three epochs. Pooling all valid focal-plane pixels, this late-to-early residual has $\sigma_{68} = 0.264\%$, with scatters of 0.246–0.291% across all detectors. Its absolute residuals have $P_{95}(|\Delta \ln S|) = 0.534\%$ and $P_{99}(|\Delta \ln S|) = 0.734\%$ (Fig. B.1). The late-to-early residual map in Fig. B.1 shows detector-boundary structures with positive residuals, compact positive regions, and several extended features. The selected compact positive regions have a median area-equivalent diameter of 5.4 pixels and a median local contrast of 0.22%. Their selection and the measurements of other residual structures are described in Appendix B.2.

The residuals include statistical uncertainty in master-flat construction and possible contributions from the calibration source, persistence, and processing. We have not subtracted a measurement-noise term. The reported scatters therefore measure repeatability of the delivered master flats, not intrinsic detector evolution. Changing the smoothing scale to 32 or 128 pixels alters the final reference-relative scatter by less than 1% relative to the nominal result. The sub-percent temporal scatter is consistent with a fixed small-scale PRNU correction for DR1.

3.2.2. Background estimation

For the background estimation step of the DR1 processing, the `GNUastro` tool `NoiseChisel` v0.16 (Akhlaghi & Ichikawa 2015) has been used, replacing `SourceExtractor` (Bertin & Arnouts 1996), which was initially part of the NIR preparation of the Q1 data release (NIRQ1).

`NoiseChisel` estimates the background by first applying a quantile threshold (set to 0.3 or 30th quantile) to create a binary map in which pixels above the threshold are marked as foreground. The thresholded image then undergoes a series of

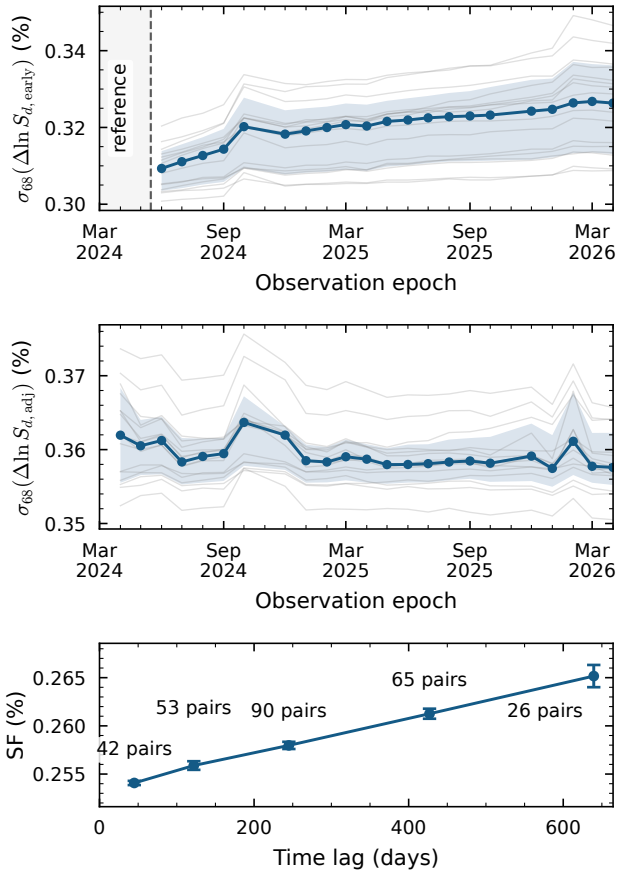


Fig. 3. Small-scale flat-field stability. *Top:* The scatter relative to the pixel-wise median of the first three epochs. The shaded interval marks those reference epochs; only subsequent measurements are plotted. *Middle:* Adjacent-epoch repeatability of the small-scale flat-field. Thin grey curves represent individual detectors, blue curves show the median across detectors, and shaded bands span the 16th–84th detector percentiles. *Bottom:* The structure function defined in Eq. (6). Error bars are leave-one-epoch-out jackknife standard errors; labels give the number of distinct epoch pairs in each lag bin. All ordinates are percentages.

morphological operations, including erosion, opening to remove isolated clumps, and dilation to recover faint source signal. This produces a final source mask. After the pixels from this mask are excluded, the image is tessellated into tiles (set to a size of 10×10 pixels), and the background in each tile is computed from the remaining sky pixels. The background estimates in each tile are then interpolated across the image using a Manhattan-distance-based nearest-neighbour scheme[1], and smoothed with a flat kernel set to a width of 3 pixels. This configuration was found to provide the best compromise between preserving the surface brightness of faint, extended sources, and minimising residuals associated with bright objects. Additionally, and similarly to what was done for the Q1 NIR processing, the estimated background is not directly subtracted from the corresponding scientific image, but is provided as a companion file.

A demonstration of the quality of the background subtraction is shown in Fig. 4, where the subtraction is performed using the `SourceExtractor` and `NoiseChisel` estimated backgrounds in the middle and right panels respectively. The improvement is visible in the preservation of faint light and low surface-brightness features surrounding the galaxy. Furthermore, the subtraction of the background reveals a faint striping pattern within the images, which is attributed to $1/f$ noise in the detector readout. This effect will be treated and integrated within the background estimation scheme for the forthcoming release (DR2), enabling a more homogeneous image background while maximising the preservation of source brightness.

[1] See the GNUastro documentation on interpolation.

Table 1. Comparison of PSF and aperture photometry for Q1 and DR1.

Band	Slope		RMS [mag]	
	Q1	DR1	Q1	DR1
Y_E	0.0192 ± 0.0028	0.0040 ± 0.0008	0.074	0.017
J_E	0.0045 ± 0.0010	0.0017 ± 0.0005	0.026	0.011
H_E	0.0024 ± 0.0006	-0.0019 ± 0.0004	0.018	0.010

3.2.3. PSF modelling from data

For Q1, the NIR PF derived the PSF models on-the-fly during the processing of each individual image (NIRQ1). While this approach allowed the PSF to be estimated directly from the data being processed, the limited number of suitable sources available in a single exposure constrained the accuracy that could be achieved, particularly in reproducing the PSF wings. In some cases, this also resulted in an unstable solution at the level of individual detectors. For DR1, the PSF-modelling strategy has been revised (Euclid Collaboration: da Silva et al. 2026), and the PSF for individual images is now derived in advance using a dedicated set of observations of the self-calibration field, comprising 76 dithers (Euclid Collaboration: Schirmer et al. 2026a). The larger and more homogeneous data set provides a significantly improved constraint on the PSF, resulting in more accurate models and enhanced stability. The resulting PSF models are stored in the Euclid Archive System (EAS) and retrieved at run time by the NIR PF when processing the science images.

In the following, we provide a brief description of the new PSF-modelling approach and present its main results, while referring the reader to the dedicated paper (Euclid Collaboration: da Silva et al. 2026) for a detailed description of the methodology and its validation, including the analysis of possible PSF spatial, colour, and temporal variations.

`SourceExtractor` (Bertin & Arnouts 1996) is used to detect and select suitable point-like sources from individual images, while `PSFEx` (Bertin 2011) is employed to derive the corresponding PSF models. The Q1 data were used to support the development of the PSF-modelling and catalogue-extraction modules of the NIR PF, as well as to refine the PSF models in preparation for DR1.

The procedure of fitting the PSF profile, compared to other methods used for flux estimation, such as aperture photometry, indicates that the PSF models under production for DR1 are better than those derived from Q1 data. In Euclid Collaboration: da Silva et al. (2026), a comparison was made between `MAG_PSF` and `MAG_APER`, both magnitudes provided by `SourceExtractor`, as a function of `MAG_APER` for magnitudes in the range 17–21. When going from Q1 to the DR1 data and using an improved version of the PSF and catalogue extraction modules (Sect. 3.2.5), the results, summarised in Table 1, show a reduction in photometric residuals by a factor 2 to 5 for the three filters, and improved consistency between the two types of photometry across the magnitude range.

The PSF models based on the stacked frames were not among the data products delivered in Q1, and no particular

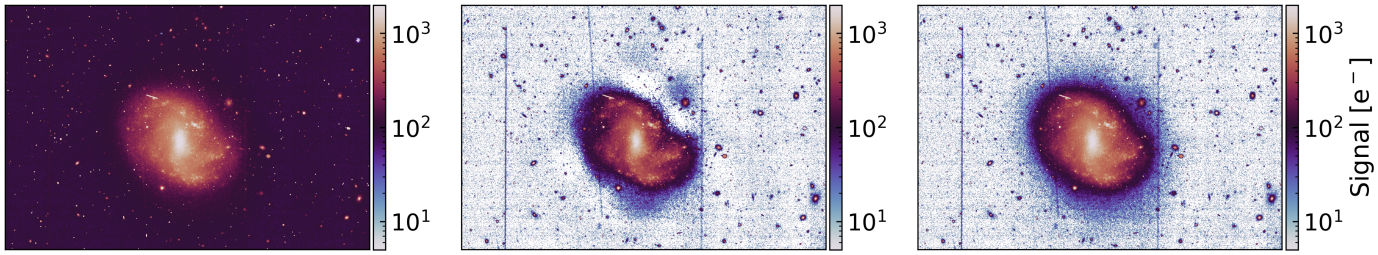


Fig. 4. *Left:* A 750 × 500-pixel section of a *Euclid* NIR image in the J_E band containing the barred spiral galaxy NGC 1483. *Middle:* The same image after background subtraction using the background estimated by `Source-Extractor`. *Right:* The background-subtracted image using the sky background estimated by `NoiseChisel`, showing the improved preservation of faint light surrounding the galaxy.

changes have been included for DR1. However, the same improvements implemented in the catalogue-extraction module for single frames can be adopted for stacked frames. By performing a similar comparison as described above, preliminary results do not suggest significant improvements in the distributions of the residuals. Tuning of the `PSFEx` parameters is expected to improve results further, and is planned for future releases.

3.2.4. Astrometric calibration

A detailed description and analysis of the results for the DR1 astrometric calibration is presented in Euclid Collaboration: Radovich et al. (2026); here, we provide only a short summary. As in Q1, the astrometric calibration in DR1 is based on `SCAMP` (Bertin 2006). The astrometric solution is obtained by using the PSF centres of sources detected by `SourceExtractor`, along with reference positions from the *Gaia* DR3 catalogue, which have been adjusted for proper motion to match the dither epoch (Gaia Collaboration: Vallenari et al. 2023). A third-order polynomial is fitted to each detector, minimising the sum of squared positional differences between matched sources both from the *Gaia* reference stars, and those detected in overlapping exposures. The robustness of the matching process is enhanced by employing an initial distortion (pre-solution), which is based on observations from the self-calibration field. In DR1, only two minor changes were made compared to Q1. (i) Before the astrometric calibration, an additional step was introduced to identify exposures that pose problems for accurate astrometric calibration, such as failures in the Fine Guidance Sensor that result in elongated source images or energetic particle showers that produce an extremely high number of spurious detections. (ii) To transfer the pre-solution to each dither, it is essential to consider the dither's rotation on the sky. This is achieved by converting the pre-solution into the simple image polynomial (SIP) formalism (Shupe et al. 2005), and then back to PV adjusting the CD matrix to account for the instrument rotation. In Q1, this transformation was achieved through polynomial fitting, while in DR1, an analytic conversion is employed.

3.2.5. Catalogue production

In the DR1 version of the catalogue extraction step, we implemented a multi-aperture photometry approach that provides flux measurements using a set of concentric apertures with radii of 0.6, 0.9, 1.5, 2.25, and 3″ (corresponding to diameters of 4, 6, 10, 15, and 20 pixels). Multi-aperture photometry is important for accurately characterising sources with different spatial extents. Small apertures provide robust flux measurements for compact sources while minimising background contamination, whereas larger apertures capture a larger fraction of the flux from extended sources and provide a more reliable estimate of their total integrated brightness. The resulting flux growth curves also allow us to quantify flux losses in small apertures, estimate the encircled energy fraction, and assess the source spatial profile relative to the PSF. These measurements are therefore relevant both for photometric calibration and for the characterisation of source morphology.

We also tuned task parameters, resulting in a more effective rejection of spurious detections and improved PSF-fitting photometry. The Q1 code version was optimised using simulations and data from *Euclid*'s PV phase (Euclid Collaboration: Schirmer et al. 2026a). While fixed-aperture photometry provided satisfactory results, the PSF-fitting photometry showed systematic biases. One of the main issues was the use of a high initial detection threshold, which led to an underestimation of the source extent in the source map. `SourceExtractor` uses this source map to define the region over which the PSF model is fitted; consequently, underestimated source sizes resulted in biased flux measurements (see sect. 3.2.6 in NIRQ1). In the DR1 version, the initial detection threshold was lowered from 5 to 2, allowing the algorithm to converge adaptively towards a more appropriate threshold and hence improving the PSF-fitting results. This improvement is illustrated by the comparison of the two plots in Fig. 5, which shows the results obtained in the Y_E band. A detailed description of the development and performance of the PSF and catalogue extraction modules of the NIR pipeline, including results for all three NISP bands, is presented in Euclid Collaboration: da Silva et al. (2026).

Two additional selection criteria, `FLUX_RADIUS` > 0.65 and `FWHM_IMAGE` > 0, were introduced to improve the rejection of spurious detections by exploiting the signal-to-noise ratio and measured size of the detected sources. In particular, since the NIR source catalogues are also used to generate several calibration products, we adopted a conservative selection criterion requiring the `SourceExtractor` quality flag to be null. This criterion removes potentially problematic, yet valid, detections from the source catalogue, including blended sources.

3.3. Resampling and stacking of NISP images

In this section, we describe the processing elements (PEs) in the NIR PF that are designed to combine single-epoch images of the same field and filter into a co-added frame. The corresponding activity diagram is shown in Fig. 6. This represents a new addition to the pipeline, since these processing steps and the associated data products (DPs) were not included in the Q1 release.

The last PE is dedicated to the creation of the output DPs, represented as yellow boxes in Fig. 6.

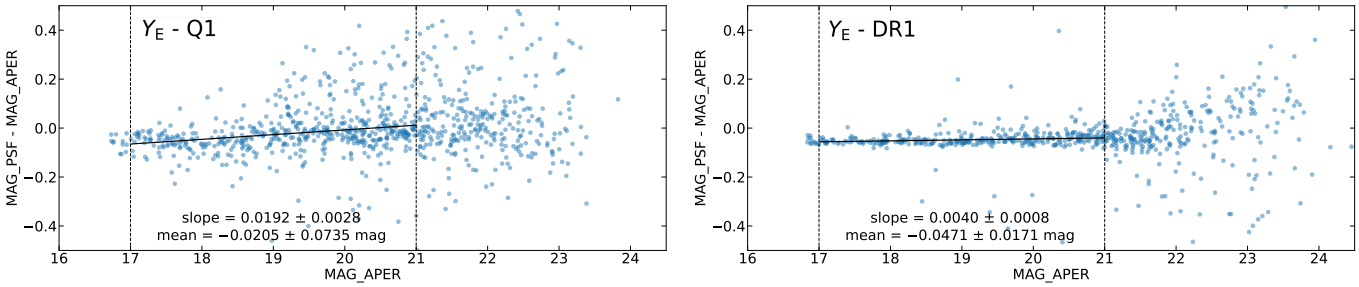


Fig. 5. NIR PF Catalogue Extraction: Comparison of PSF-fitting and aperture photometry (`MAG_PSF − MAG_APER`) for the Y_E band across Q1 (left panel) and DR1 (right panel) versions of code and PSF models.

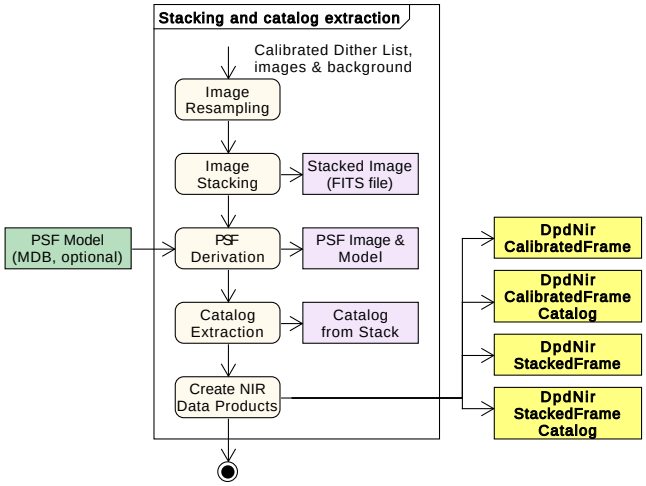


Fig. 6. NIR PF resampling and stacking. The last PE is dedicated to the creation of the final DPs, represented as yellow boxes, that are stored into the EAS.

In addition to the calibrated single-epoch image, `DpdNirCalibratedFrame`, and its corresponding source catalogue, `DpdNirCalibratedFrameCatalog`, already released for Q1 (NIRQ1), the NIR PF in DR1 produces two new DPs: the stacked image, `DpdNirStackedFrame`; and its corresponding source catalogue, `DpdNirStackedFrameCatalog`. Detailed information on the definition of the NIR DPs for DR1 are reported in Appendix C.

3.3.1. Resampling

The main goal of the `NIR_resampling` module is to realign, rotate, and resample onto a common grid the 16 detector images from the dither exposures acquired in the same field and with the same NISP-P filter. The astrometrically and photometrically calibrated images are first background-subtracted using the background estimates described in Sect. 3.2.2, and then processed using `SWarp` (Bertin et al. 2002), which projects each detector image onto a common grid. `SWarp` uses an inverse-mapping technique: the output frame is scanned pixel by pixel, and the position of each output pixel in the input frame is determined through the inverse geometrical transformation. Since the resulting coordinates generally do not coincide with the input pixel grid, the corresponding pixel value is estimated by interpolating the values of neighbouring input pixels. This approach ensures that every pixel in the output frame is assigned a value, avoiding the gaps that may arise with forward-mapping techniques.

Table 2. Parameters in the `SWarp` configuration file (Bertin 2010) used by the resampling module.

`SWarp` Parameter	Value
`FSCALE_KEYWORD`	set at runtime
`FSCALASTRO_TYPE`	`VARIABLE`
`OVERSAMPLING`	5
`RESAMPLING_TYPE`	`LANCZOS2`
`WEIGHT_TYPE`	`MAP_VARIANCE`
`COMBINE_TYPE`	`WEIGHTED`

We tested nearest-neighbour, bilinear, and Lanczos-2, -3, and -4 interpolation functions (Bertin 2010) by comparing the magnitude and centroid differences of extracted sources before and after resampling. Lanczos-2 provides a good compromise, yielding a mean signed difference of less than 0.005 mag in magnitude and an RMS of 0.″015 in both RA and Dec, while introducing fewer artefacts around image discontinuities. For comparison, bilinear interpolation yielded a mean signed difference of 0.010 mag and RMS residuals of 0.″020 in both RA and Dec. Lanczos-3 performed slightly better in terms of accuracy, with a mean signed difference of 0.003 mag and RMS residuals of 0.″010, but its larger 6×6-pixel kernel significantly increased the number of flagged pixels. Resampling is performed with an oversampling factor of 5, with fluxes rescaled according to the local pixel-scale ratio, and the inverse variance maps of the input dithers are used as weights. An additional flux scaling factor, accounting for the exposure time and the inverse sensitivity associated with each NISP-P filter (Sect. 4.4), is computed during resampling and applied when stacking the individual frames to convert the fluxes to the adopted AB magnitude system.

The resampled images from each detector and dither exposure are combined into a multi-extension FITS (MEF) file preserving the three-layer structure – image (SCI), RMS, and data quality (DQ) – of the input dithers (NIRQ1). Flags from the DQ layer are also propagated. Since this functionality is not available in the official version of `SWarp`, we use a dedicated C++ version of the code. Overlapping adjacent pixels are combined using the OR operator: if the flags are identical, the original flag is retained; if they differ, the resulting flag is the bit-wise sum of the two flag values. The resampled variance layer is obtained as the inverse of the resampled weights.

3.3.2. Stacking

The astrometrically and photometrically calibrated dither exposures for a given field and filter, previously resampled onto a common grid, are combined into a single stacked image using `SWarp`. As for the resampling, the stacking procedure is also

controlled by a set of parameters defined in the configuration file. The `COMBINE_TYPE` parameter specifies how the input images are combined. We tested several options and found that the 'weighted' and 'median' methods provide the best results by visual inspection. The parameter is currently set to 'weighted', while `WEIGHT_TYPE` is set to 'map_weight'. With this configuration, for each output pixel, `SWarp` combines the corresponding values from all input images, weighting them according to the resampled weight maps.

The current version of the `NIR_stacking` module also supports the propagation of flags stored in the DQ layer. This functionality is implemented using the C++ version of `SWarp`. Flags from different dithers are combined using the OR operator as for the resampling step. Flag propagation is controlled by a boolean input port, which is currently set to 'false', but can be enabled if needed.

The combined frames are stored in a three-layer (SCI, RMS, and DQ) MEF file. The co-added RMS layer is computed as the square root of the co-added variance, which is obtained as the inverse of the co-added weights. For zero weights, the variance is set to 10^{16}, which is significantly higher than the variance of valid pixels, ensuring that they are effectively excluded from the weighted stacking without introducing numerical issues. Since flag propagation is currently disabled, the co-added DQ layer is derived from the co-added weights by setting pixels with zero weight to 1 and all other pixels to 0. Finally, the headers of the MEF files are populated with the keywords required by the Euclid Common Data Model.

4. Results for Euclid Data Release 1

4.1. Accuracy of the astrometric calibration

The astrometric performance and the limitations identified during the DR1 processing are described in detail in Euclid Collaboration: Radovich et al. (2026). The achieved accuracy is well within the requirement of 30 mas. When all detections in a given dither are considered, the offsets with respect to *Gaia* are within 2 mas; the average RMS is 10 mas and remains below 20 mas for 99% of the dithers in all bands. Similar values are obtained when considering overlaps across dithers in each band.

During DR1 processing, the more conservative approach adopted to flag pixels potentially affected by persistence sometimes resulted in a notable decrease in the number of sources with matches in the *Gaia* catalogue, from approximately 30 per detector to just a few. This effect was particularly noticeable for detectors DET13 and DET14 (see Euclid Collaboration: Jahnke et al. 2025 for the definition of the detector's slot). Consequently, this could lead to a local reduction in astrometric accuracy to above 50 mas for those two detectors (see also Euclid Collaboration: Schirmer et al. 2026a). While the issue was resolved, the corresponding correction could not be implemented in DR1 and will instead be applied in DR2. A comparative analysis with the VIS catalogues indicates that this issue impacts approximately 3% and 0.3% of the total DR1 area, with RMS thresholds of 30 mas and 60 mas, respectively. Regions affected by this issue can be identified by VMPZ-ID `InfoMaps` (Euclid Collaboration: Odier et al. 2026), which are based on the RMS maps also described in Euclid Collaboration: Radovich et al. (2026).

4.2. Stability of the NISP throughput

Similarly to Q1, we take advantage of the monthly visits to the self-calibration field to monitor the stability of the NISP throughput and adjust the photometric zero point to maintain the relative calibration within the required 1.5% accuracy. In addition to monitoring the white dwarf (WD) primary calibrator WDJ175318.65+644502 (Sect. 4.4), we follow the procedure described in section 5.2 of NIRQ1 to compute magnitude differences for each visit, adopting the self-calibration field observation from June 2024 as the reference epoch, which corresponds to the observation immediately following the second decontamination procedure (Euclid Collaboration: Schirmer et al. 2026b). The results shown in Fig. 7 indicate variations of a few percent in the NISP throughput in all three NIR filters. These variations are consistent with the formation of ice on the detectors (Euclid Collaboration: Schirmer et al. 2026a). It is worth noting that, during each self-calibration visit, the WD is observed on only a limited number of detectors. Consequently, the error bars on the WD zero points include a systematic uncertainty contribution arising from residual detector-to-detector offsets.

To improve the consistency of flux measurements throughout the DR1 period, we adopted a step-wise approach, selecting a set of inverse sensitivity (IS) values that track the throughput evolution derived from all sources in the self-calibration field, as shown in Fig. 7. The resulting zero-point residuals are shown in the right panel of Fig. 7, together with additional measurements from the contamination monitoring programme that was executed on the centre of the self-cal field during early science operations (F-014, see table D.1 in Euclid Collaboration: Schirmer et al. 2026a). Since F-014 observations are based on a sequence of four dithers instead of 76, they are not suitable for deriving calibration products, but provide a useful independent data set for monitoring zero-point residuals. Figure 7 shows that the adopted calibration products provide a temporal stability of the NISP photometric relative calibration that complies with the 1.5% requirement. For most of the survey, the residuals remain at the level of approximately 2 mmag. The main exception is the period between November 2023 and March 2024, during which no observations of the self-calibration field suitable for deriving calibration products were performed. In DR2, a smooth interpolation model will be used to describe the throughput evolution at any time in the survey.

4.3. Accuracy of the relative photometric calibration

The same observations of the self-calibration field used to monitor the overall NISP throughput are also exploited to assess the accuracy of the NIR relative photometric calibration. For each source, we extract individual photometric measurements from all exposures of all self-cal visits, and compute the median flux and the median absolute deviation (MAD). These statistics are then analysed as a function of source magnitude to assess the photometric repeatability and identify any magnitude-dependent systematics.

The results are shown in Fig. 8 for the $J_{\rm E}$ band, and include statistical and systematic residual effects from ice contamination and unmasked persistence. At the bright end, where the measurements are not dominated by shot noise, the scatter of the repeated measurements corresponds to a relative flux calibration uncertainty of 0.9%, compared to a requirement of 1.5%. Similar results are obtained for the $Y_{\rm E}$ and $H_{\rm E}$ bands. It should be noted that all self-calibration field visits are analysed together; therefore, the measured scatter also accounts for any potential time-dependent variations in the photometry.

The same data set can also be exploited to investigate potential spatial systematics by analysing photometric residuals as a function of detector position (x, y) within the FPA, using

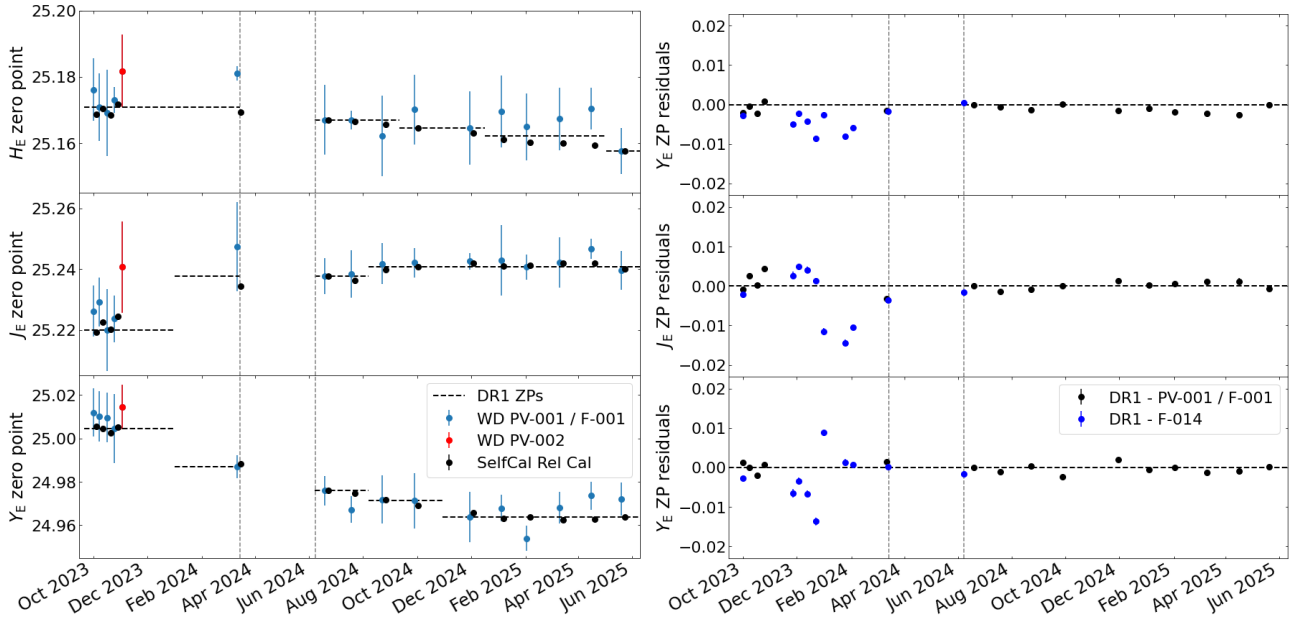


Fig. 7. *Left:* Monitoring of the NISP zero-point evolution using both the WD calibrator (blue and red points) and the combination of all sources (black points) from the monthly self-calibration field visits. Black dashed lines represent the zero points adopted for DR1. *Right:* Residuals for the NISP zero points throughout the DR1 period. Results are compatible with the 1.5% requirement on relative photometric calibration.

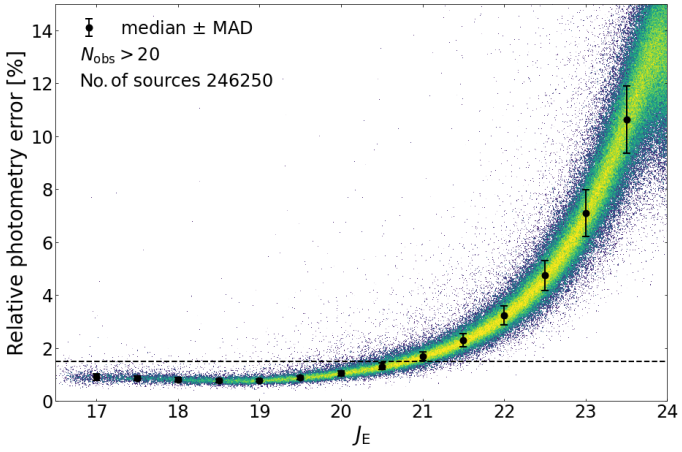


Fig. 8. Relative flux calibration uncertainty for J_E estimated from all visits of the self-calibration field. The error for sources brighter than 19 mag is at the level of 0.9%. Similar results are obtained for Y_E and H_E. The dashed line shows the 1.5% requirement (maximum allowed post-calibration error).

catalogue-level magnitude measurements from individual observations of the self-calibration field. The residuals are defined with respect to the mean magnitude of each source and projected onto the focal plane according to their detector coordinates.

Two-dimensional maps of the residuals are constructed by binning the measurements in detector coordinates and computing the median within each spatial bin. This approach mitigates the impact of outliers and enables the identification of coherent spatial structures across the detector.

The resulting residual maps are inspected for large-scale features that may reveal instrumental effects not fully corrected by the NIR PF or the adopted calibration products. The analysis benefits from the high redundancy of the self-calibration field, where repeated measurements of the same sources sample different regions of the detector. Results for the full data set, shown in Fig. 9, indicate that residual spatial features are at the level of 0.01 mag or below.

When restricting the analysis to bright sources, however, the spatial distribution of the residuals across the FPA reveals the features shown in Fig. 10, which closely resemble the persistence charge patterns shown in figure 4 of NIRQ1. This suggests that the flux-dependency of persistence parameters discussed in Euclid Collaboration: Kubik et al. (2026), and in particular the different behaviour in the bright and faint regimes, may provide an explanation for these features, as also noted in NIRQ1. Indeed, in terms of source counts, bright objects provide only a subdominant contribution to the large-scale flat-field estimation compared to the full source population.

4.4. Accuracy of absolute photometric calibration

As discussed in NIRQ1, we adopt the faint spectrophotometric white dwarf WDJ175318.65+644502.15 (*Gaia* source ID 1440758225532172032), whose flux is tied to *Hubble* Space Telescope (HST) CALSPEC (Bohlin et al. 2014, 2017, 2020), as the primary calibrator for the flux calibration of the *Euclid* NISP imaging. During the DR1 period, three other *Euclid* spectro-photometric WDs were observed (Euclid Collaboration: Schirmer et al. 2026a; Deustua et al., in prep.), two in the EDF-North and one in EDF-South (Euclid Collaboration: Tereno et al. 2026; Euclid Collaboration: Scaramella et al. 2022). Figure 11 shows the positions of these three white dwarfs, together with that of WDJ175318.65+644502.15, relative to the footprints of the EWS and EDS, while Table 3 summarises their coordinates and the NIR fluxes.

All three standards are tied to CALSPEC and have both photometric and spectroscopic HST observations obtained with WFC3/IR and STIS under programmes 16702 (PI: Appleton) and 17442 (Deustua). The hot WDs were originally selected from the *Gaia* DR2 WD candidate catalogue (Gentile Fusillo et al. 2019) by requiring a temperature of $T > 11\,000$ K, in order to exclude potentially variable cool WDs

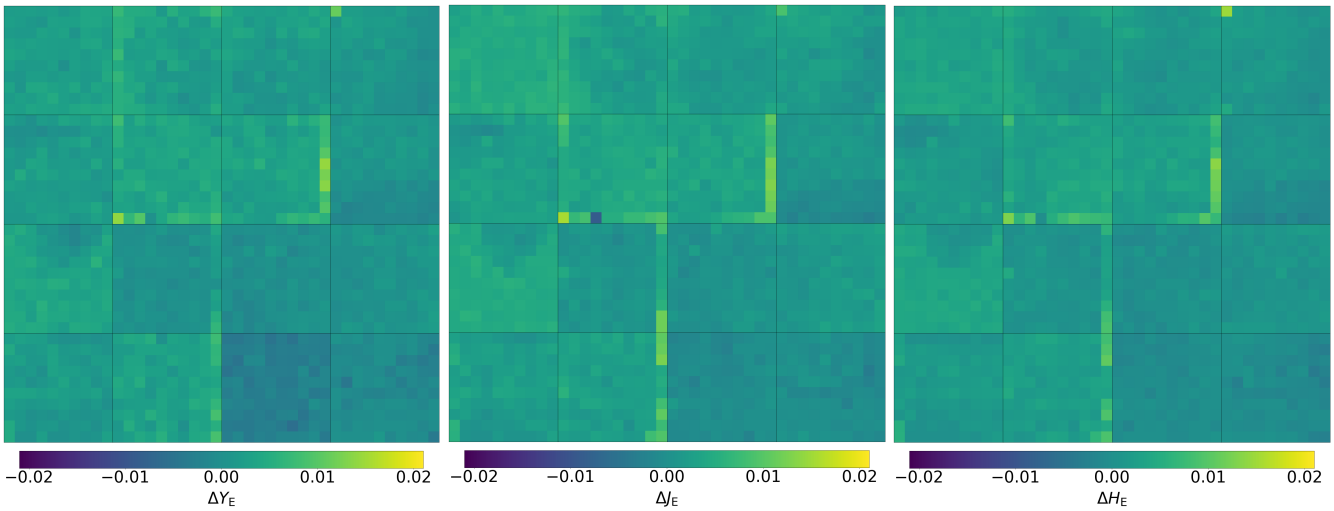


Fig. 9. FPA distribution of photometric residuals for Y_E, J_E, and H_E combining all observations of the self-calibration field during the DR1 period.

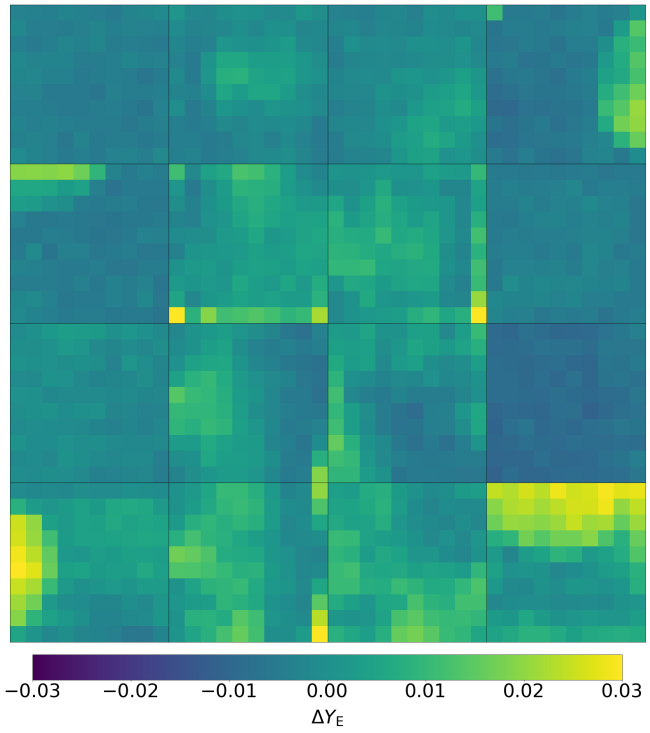


Fig. 10. FPA distribution of photometric residuals for Y_E when considering only sources with $17 < Y_E < 19$. Similar results are obtained for J_E and H_E.

(Deustua et al., in prep.). Long- and short-term monitoring showed stability at the level of 1% or better. Observations of WDJ175318.65+644502.15 with VIS at optical wavelengths show that this particular standard in the self-cal field is probably more variable than initially thought; DR2 absolute flux calibration will be based on a sufficiently larger number of spectrophotometric standards (Euclid Collaboration: Schirmer et al. 2026a).

Following the analysis described in detail in NIRQ1, we derive the absolute flux calibration factor, or IS, for these three additional white dwarfs and compare their values with that obtained for our primary calibrator, WDJ175318.65+644502.15. To assess the accuracy and temporal stability of the calibration, we examine the IS values as a function of observation time, thereby accounting for potential temporal variations in filter throughput and photometric zero points.

Table 3. Spectrophotometric white dwarfs used for flux calibration and validation.

ID	RA	Dec	H_{AB}
WDJ175318+644502	17:53:18.65	+64:45:02.15	18.36
WDJ174911+643533	17:49:11.78	+64:35:33.54	18.26
WDJ181144+654916	18:11:44.96	+65:49:16.42	19.14
WDJ041345−473726	04:13:45.06	−47:37:26.29	18.27

Figure 12 shows the IS measurements for all four WDs in the three NISP bands. We restrict the time range to June 2024 through June 2025 to ensure sufficient temporal overlap among the comparison WDs. The primary calibrator, WDJ175318.65+644502.15, is shown in green. For each WD, the median IS value over the full time range is indicated by a solid line, with the line colour matching that of the corresponding data points. The shaded green region represents the $2\,\sigma$ scatter around the median IS of the primary calibrator. The scatter, σ, is estimated using the scaled median absolute deviation (SMAD), defined as SMAD = $1.4826 \times$ MAD, where MAD is the median absolute deviation. As shown in the figure, the median IS values of the other three WDs lie well within the $2\,\sigma$ scatter of the primary calibrator. The dotted magenta line indicates the mission-required 5% boundary.

5. Discussion

This paper has presented the NIR PF used to process the NISP raw photometric exposures for DR1. The analysis of the resulting calibrated single-epoch catalogues demonstrates that the main requirements for astrometric and photometric calibration are met. At the same time, a detailed validation of the images has highlighted a number of residual effects and limitations. While these do not compromise the robustness of the scientific results obtained for the *Euclid* DR1 core science programmes, they may be relevant for other scientific applications and analyses, such as low surface-brightness and galaxy-cluster studies. Their characterisation is therefore important for the proper interpretation of the data and their broader scientific exploitation, as well as to guide further improvements to the NIR data products in view of

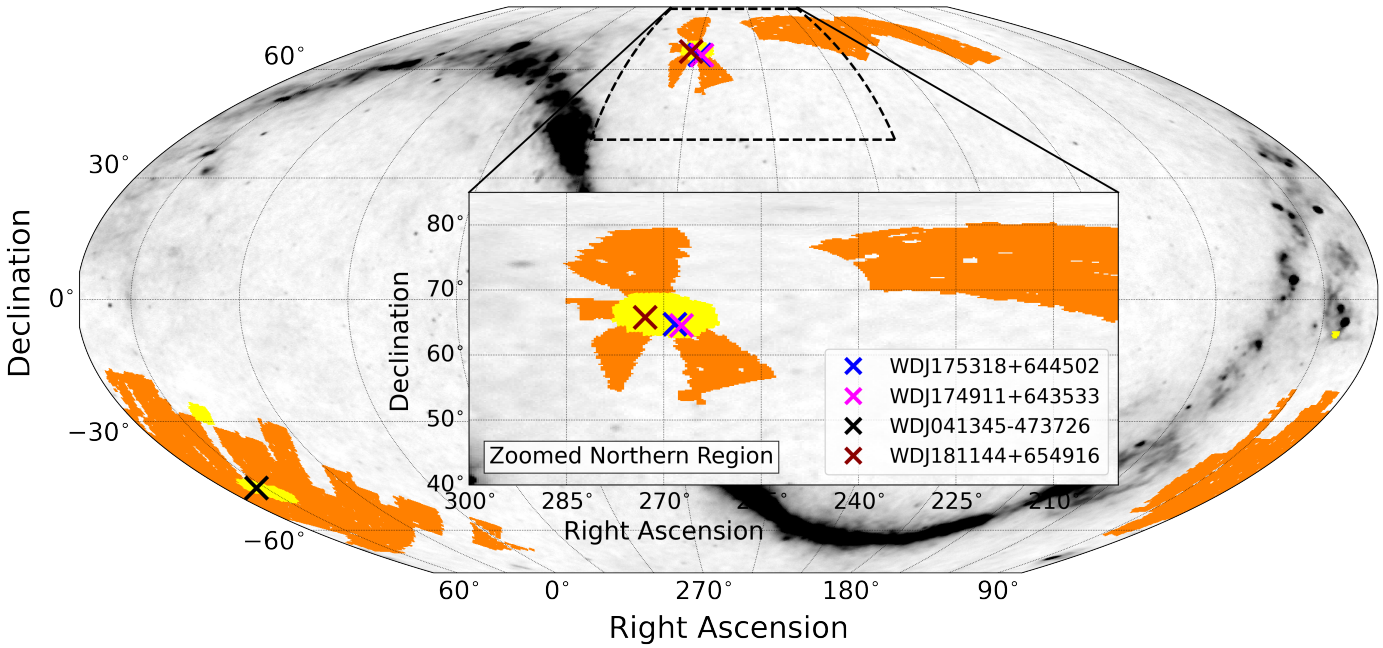


Fig. 11. Full-sky map showing the positions of the four spectrophotometric WDs observed during the DR1 campaign. The main WD calibrator used for the NISP absolute flux calibration is shown with a blue cross. The DR1 and Q1 coverages are shown in orange and yellow, respectively.

future releases, which will encompass larger datasets and require increasingly stringent levels of accuracy.

- Persistence. Although persistence modelling has improved significantly for DR1, it does not yet capture the full complexity of the effect (Euclid Collaboration: Kubik et al. 2026), limiting the accuracy of procedures aimed at correcting the associated excess flux (Awad et al., in prep.). Therefore, a masking approach is preferred over attempting to correct the persistence signal. Tracing a 5-hour illumination history improves the ability to identify and mask residual streaks from spectroscopic observations. However, in some cases, this approach results in excessive masking. In particular: (i) in the presence of proton showers, energetic particle hits could remain masked for an extended period, causing the accumulation of masked regions and leading to the invalidation of several images; (ii) for DET13 and DET14, the masking results in the astrometric issues described in Sect. 4.1. Although a solution has already been identified, it could not be implemented for DR1. VMPZ-ID `InfoMaps` are therefore provided to identify the affected regions.
- Background estimation. As shown in Fig. 4, while the outskirts of extended sources are preserved, residual horizontal stripes due to $1/f$ noise in the detector readout are still present. This is a known effect also observed in JWST/NIRCam data (Space Telescope Science Institute 2025) and will be addressed for DR2. We find that, when stacking a large number of background frames, the resulting master background shows spatial patterns similar to those seen in the persistence images and in the photometric residuals of bright sources shown in Fig. 10. This indicates that the large-scale flat derived from source fluxes does not completely remove the corresponding background structure, consistent with the different levels of persistence contamination in the bright and faint regimes. When the dithering pattern is insufficient to average out these residual structures, they can result in an excess of diffuse faint signal. Finally, since the background is estimated independently for each detector, its uniformity on larger, focal-plane scales is not guaranteed.
- Relative and absolute photometric calibration. When considering the full sample of sources, the focal-plane distribution of photometric residuals shows no evidence of spatial features with a dispersion above the 0.01 mag level. However, spatial structures become apparent when restricting the analysis to bright sources only. The absolute calibration is tied to a single-epoch observation of WDJ175318.65+644502.15, while the other secondary WDs observed by *Euclid* are used for validation only and not used to improve the calibration accuracy. Temporal variations in the throughput due to the presence of ice are accounted for by adopting a set of IS values in a step-wise approach. While the resulting residuals remain within the *Euclid* requirements, this approach leaves room for further improvement. Moreover, the presence of ice affects the 16 NISP detectors differently. This is accounted for through the monthly estimation of detector offsets from self-calibration field observations, together with the large-scale flat. Inter-detector variations are not corrected, although the analysis presented in Sect. 3.2.1 suggests that their impact is well below 1% over most of the focal plane.
- Unmodelled instrumental effects. These include spikes from bright stars and snowballs, which are partially masked during pre-processing, although no dedicated masking step is currently implemented. Arcs from bright stars (see figure 21 in Euclid Collaboration: Jahnke et al. 2025) are not masked in DR1. Current investigations show the arcs are generally caused by bright stars within a particular area on the FPA. From the DR1 data, preliminary work indicates that around 3% of images show these arcs, with the exact position and shape dependent on the position of the bright star causing them. The exact optical surfaces causing these arcs and a model to describe them in order to provide masks, are under investigation and planned for future releases.

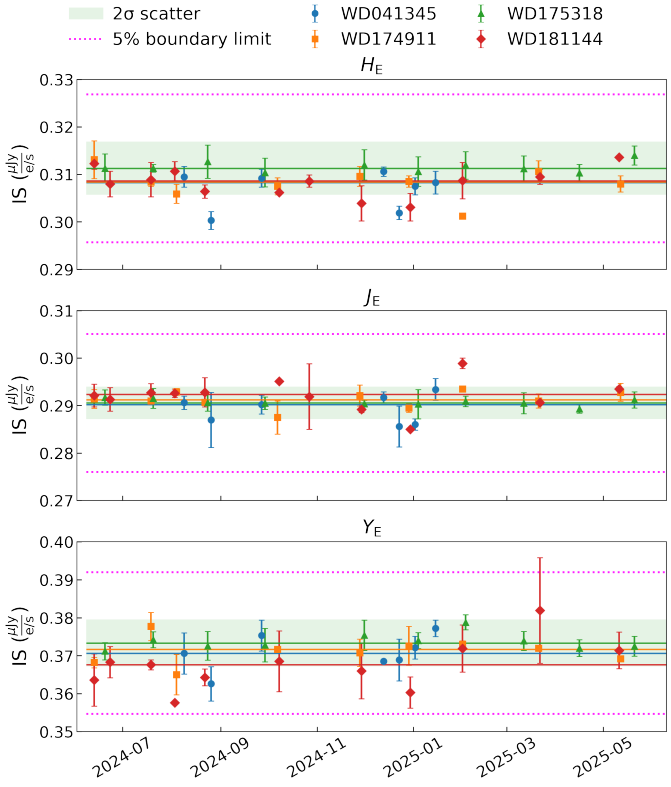


Fig. 12. Inverse sensitivity as a function of observation time. The IS measurements of the four hot WDs, including the main calibrator WDJ175318.65+644502.15, used for NISP absolute flux calibration are shown within the time range of June 2024 through June 2025. The median value of IS measurements for the other three WDs are well within the $2\,\sigma$ scatter range of the main calibrator. We describe in the text how the scatter, σ, is measured using SMAD.

The analysis presented in this paper has identified a number of residual effects and limitations in the DR1 processing. Nevertheless, the results confirm that the DR1 NIR data products meet the required levels of astrometric and photometric accuracy and provide a robust basis for the scientific exploitation of the *Euclid* data. The improvements being developed for DR2 are expected to further mitigate these effects and improve the quality and consistency of the NIR data products.

Acknowledgements. The Euclid Consortium acknowledges the European Space Agency and a number of agencies and institutes that have supported the development of *Euclid*, in particular the Agenzia Spaziale Italiana, the Austrian Forschungsförderungsgesellschaft funded through BMIMI, the Belgian Science Policy, the Canadian Euclid Consortium, the Deutsches Zentrum für Luft- und Raumfahrt, the DTU Space and the Niels Bohr Institute in Denmark, the French Centre National d'Etudes Spatiales, the Fundação para a Ciência e a Tecnologia, the Hungarian Academy of Sciences, the Ministerio de Ciencia, Innovación y Universidades, the National Aeronautics and Space Administration, the National Astronomical Observatory of Japan, the Nederlandse Onderzoekschool Voor Astronomie, the Norwegian Space Agency, the Research Council of Finland, the Romanian Space Agency, the Swiss Space Office (SSO) at the State Secretariat for Education, Research, and Innovation (SERI), and the United Kingdom Space Agency. A complete and detailed list is available on the *Euclid* web site (www.euclid-ec.org/consortium/community/). This work has made use of the *Euclid* Data Release 1 (DR1) from the European Space Agency (ESA) mission *Euclid*, available at https://www.cosmos.esa.int/web/euclid/data-release-dr1. This work has made use of data from the European Space Agency (ESA) mission *Gaia* (https://www.cosmos.esa.int/gaia), processed by the *Gaia* Data Processing and Analysis Consortium (DPAC, https://www.cosmos.esa.int/web/gaia/dpac/consortium). Funding for the DPAC has been provided by national institutions, in particular the institutions participating in the *Gaia* Multilateral Agreement.

References

Akhlaghi, M. & Ichikawa, T. 2015, ApJS, 220, 1
Bertin, E. 2006, in ASP Conf. Ser., Vol. 351, Astronomical Data Analysis Software and Systems XV, ed. C. Gabriel, C. Arviset, D. Ponz, & S. Enrique, 112
Bertin, E. 2010, SWarp: Resampling and Co-adding FITS Images Together, Institut d'Astrophysique de Paris, SWarp User's Guide, version 2.21
Bertin, E. 2011, in ASP Conf. Ser., Vol. 442, Astronomical Data Analysis Software and Systems XX, ed. I. N. Evans, A. Accomazzi, D. J. Mink, & A. H. Rots, 435
Bertin, E. & Arnouts, S. 1996, A&AS, 117, 393
Bertin, E., Mellier, Y., Radovich, M., et al. 2002, in ASP Conf. Ser., Vol. 281, Astronomical Data Analysis Software and Systems XI, ed. D. A. Bohlender, D. Durand, & T. H. Handley, 228
Bohlin, R. C., Gordon, K. D., & Tremblay, P. E. 2014, PASP, 126, 711
Bohlin, R. C., Hubeny, I., & Rauch, T. 2020, AJ, 160, 21
Bohlin, R. C., Mészáros, S., Fleming, S. W., et al. 2017, AJ, 153, 234
Euclid Collaboration: Aussel, H. et al. 2026, arXiv, submitted
Euclid Collaboration: Cropper, M., Al-Bahlawan, A., Amiaux, J., et al. 2025, A&A, 697, A2
Euclid Collaboration: da Silva, R., Faustini, F., Polenta, G., et al. 2026, A&A, submitted
Euclid Collaboration: Hormuth, F., Jahnke, K., Schirmer, M., et al. 2025, A&A, 697, A4
Euclid Collaboration: Jahnke, K., Gillard, W., Schirmer, M., et al. 2025, A&A, 697, A3
Euclid Collaboration: Kubik, B., Conseil, S., Ferriol, S., et al. 2026, A&A, submitted
Euclid Collaboration: Le Brun, V., Bethermin, M., Moresco, M., et al. 2026, A&A, 711, A7
Euclid Collaboration: Mellier, Y., Abdurro'uf, Acevedo Barroso, J., et al. 2025, A&A, 697, A1
Euclid Collaboration: Odier, J., Macias-Perez, J., Alguero, G., et al. 2026, arXiv, submitted
Euclid Collaboration: Polenta, G., Frailis, M., Alavi, A., et al. 2026, A&A, 711, A3
Euclid Collaboration: Radovich, M., da Silva, R., Polenta, G., et al. 2026, A&A, submitted
Euclid Collaboration: Ruffenach, M., Frailis, M., Zacchei, A., et al. 2026, A&A, submitted
Euclid Collaboration: Scaramella, R., Amiaux, J., Mellier, Y., et al. 2022, A&A, 662, A112
Euclid Collaboration: Schirmer, M., Jahnke, K., Seidel, G., et al. 2022, A&A, 662, A92
Euclid Collaboration: Schirmer, M., Paterson, K., Alavi, A., et al. 2026a, A&A, submitted
Euclid Collaboration: Schirmer, M., Paterson, K., Altieri, B., et al. 2026b, A&A, submitted
Euclid Collaboration: Schirmer, M., Thürmer, K., Bras, B., et al. 2023, A&A, 675, A142
Euclid Collaboration: Tereno, I., Dinis, J., Dupac, X., et al. 2026, arXiv, submitted
Euclid Data Release 1. 2026, https://doi.org/10.57780/esa-d079c51
Gaia Collaboration: Vallenari, A., Brown, A. G. A., Prusti, T., et al. 2023, A&A, 674, A1
Gentile Fusillo, N. P., Tremblay, P.-E., Gänsicke, B. T., et al. 2019, MNRAS, 482, 4570
Hough, P. V. 1962, Method and means for recognizing complex patterns, US Patent 3069654
Kubik, B., Barbier, R., Smadja, G., et al. 2024, in SPIE Conf. Ser., Vol. 13103, X-Ray, Optical, and Infrared Detectors for Astronomy XI, ed. A. D. Holland & K. Minoglou, 1310315
Rauscher, B. J., Boehm, N., Cagiano, S., et al. 2014, PASP, 126, 739
Shupe, D. L., Moshir, M., Li, J., et al. 2005, in ASP Conf. Ser., Vol. 347, Astronomical Data Analysis Software and Systems XIV, ed. P. Shopbell, M. Britton, & R. Ebert, 491
Space Telescope Science Institute. 2025, NIRCam 1/f Noise Removal Methods, JWST User Documentation, https://jwst-docs.stsci.edu/known-issues/nircam-known-issues/nircam-1-f-noise-removal-methods

Authors and affiliations

Euclid Collaboration: G. Polenta[⋆1], M. Frailis[2], A. Alavi[3], P. N. Appleton[3], P. Awad[4], A. Bonchi[1], L. Bramante[5], G. Calderone[2], F. Cogato[6], S. Conseil[7,8], M. Correnti[9,1], R. da Silva[9,1], I. Das[3], F. Faustini[9], Y. Fu[4,10], T. Gasparetto[9], W. Gillard[11], S. Hemmati[3], J. Jacobson[3], K. Jahnke[12], B. Kubik[8], X. Liu[3], C. Macabiau[8], E. Medinaceli[6], P. W. Morris[13], K. Paterson[12], M. Radovich[14], M. Schirmer[12], H. I. Teplitz[15], A. Troja[2], B. P. Venemans[4], B. Altieri[16], S. Andreon[17], N. Auricchio[6], H. Aussel[18], C. Baccigalupi[19,2,20,21], M. Baldi[22,6,23], A. Balestra[14], S. Bardelli[6], P. Battaglia[6], A. N. Belikov[10,24], R. Bender[25,26], A. Biviano[2,19], E. Branchini[27,28,17], M. Brescia[29,30], J. Brinchmann[31,32,33], S. Camera[34,35,36], G. Cañas-Herrera[4], V. Capobianco[36], C. Carbone[37], V. F. Cardone[9,38], J. Carretero[39,40], F. J. Castander[41,42], M. Castellano[9], G. Castignani[6], S. Cavuoti[30,43], K. C. Chambers[44], A. Cimatti[45], C. Colodro-Conde[46], G. Congedo[47], C. J. Conselice[48], L. Conversi[49,16], Y. Copin[8], F. Courbin[50,51,52], H. M. Courtois[53], M. Cropper[54], A. Da Silva[55,56], H. Degaudenzi[57], G. De Lucia[2], H. Dole[58,59], F. Dubath[57], X. Dupac[16], S. Dusini[60], S. Escoffier[11], M. Fabricius[25,26], M. Farina[61], R. Farinelli[6], S. Ferriol[8], F. Finelli[6,62], S. Fotopoulou[63], N. Fourmanoit[11], E. Franceschi[6], M. Fumana[37], L. Gabarra[64], S. Galeotta[2], K. George[65], C. Giocoli[6,23], J. Gracia-Carpio[25], B. R. Granett[17], A. Grazian[14], F. Grupp[25,26], L. Guzzo[66,17,67], W. G. Hartley[57], S. V. H. Haugan[68], J. Hoar[16], H. Hoekstra[4], W. Holmes[69], I. M. Hook[70], F. Hormuth[71], A. Hornstrup[72,73], M. Huertas-Company[46,74,75], M. Jhabvala[76], S. Kermiche[11], A. Kiessling[69], R. Kohley[16], M. Kümmel[26], M. Kunz[77], H. Kurki-Suonio[78,79], A. M. C. Le Brun[80], V. Le Brun[81], D. Le Mignant[81], P. Liebing[54], S. Ligori[36], P. B. Lilje[68], V. Lindholm[78,79], I. Lloro[82], M. Magliocchetti[61], G. Mainetti[83], O. Mansutti[2], S. Marcin[84], O. Marggraf[85], M. Martinelli[9,38], N. Martinet[81], F. Marulli[86,6,23], R. J. Massey[87], N. Mauri[45,23], H. J. McCracken[88], C. J. R. McPartland[73,89], S. Mei[90,91], M. Meneghetti[6,23], E. Merlin[14], G. Meylan[92], P. Monaco[93,2,20,19], A. Mora[94], M. Moresco[86,6], C. Moretti[2,19,20], L. Moscardini[86,6,23], R. Nakajima[85], C. Neissner[95,40], R. C. Nichol[96], S.-M. Niemi[97], C. Padilla[95], S. Paltani[57], F. Pasian[2], J. A. Peacock[47], W. J. Percival[98,99,100], V. Pettorino[97], S. Pires[18], M. Poncet[101], L. A. Popa[102], F. Raison[25], A. Refregier[103], A. Renzi[104,60,6], J. Rhodes[69], G. Riccio[30], I. Risso[27,28,17], F. Rizzo[2], E. Romelli[2], C. Rosset[90], B. Rusholme[3], R. Saglia[26,25], Z. Sakr[105,106,107], A. G. Sánchez[25], D. Sapone[108], B. Sartoris[109], P. Schneider[85], T. Schrabback[110], M. Scodeggio[37], A. Secroun[11], E. Sefusatti[2,19,20], E. Sihvola[78,79], P. Simon[85], C. Sirignano[104,60], G. Sirri[23], L. Stanco[60], P. Tallada-Crespí[39,40], A. N. Taylor[47], I. Tereno[55,56], N. Tessore[54], S. Toft[111,89], R. Toledo-Moreo[112,113], F. Torradeflot[40,39], A. Tsyganov[114], I. Tutusaus[41,42,106], J. Valiviita[78,79], T. Vassallo[2,65], A. Veropalumbo[17,28,27], D. Vibert[81], Y. Wang[3], J. Weller[26,25], A. Zacchei[2,19], G. Zamorani[6], F. M. Zerbi[17], E. Zucca[6], I. T. Andika[26], M. Ballardini[115,116,6], P. Bergamini[6], S. Borgani[93,19,2,20,117], E. Bozzo[57], C. Burigana[118,62], R. Cabanac[106], M. Calabrese[119,37], A. Cappi[109,6], F. Caro[9], T. Castro[120,2,19], D. Di Ferdinando[23], J. A. Escartin Vigo[25], G. Fabbian[58], J. García-Bellido[105], V. Gautard[121], A. Gregorio[93,2,20], C. M. Gutierrez[46,122], A. Hall[47], Y. Kang[110], G. Leroy[123,87], A. Loureiro[124,125], J. Macias-Perez[126], C. Mancini[37], R. Maoli[127,9], R. B. Metcalf[86,6], S. Nadathur[128], L. Patrizii[23], M. Pöntinen[78], E. Sarpa[2], V. Scottez[129,130], M. Sereno[6,23], K. Tanidis[131], M. Tenti[23], M. Tucci[57], M. Viel[19,2,21,20,117], M. Wiesmann[68], Abdurro'uf[132], J. A. Acevedo Barroso[69], Y. Akrami[105,133], G. Alguero[126], G. Angora[30,115], S. Anselmi[60,104,134], M. Archidiacono[66,67], G. Aricò[23], F. Atrio-Barandela[135], M. Aubert[8], M. Baes[136], N. Bartolo[104,60,14], L. Bazzanini[115,6], J. Bel[137], J. R. Bermejo-Climent[138,139], D. Bertacca[104,14,60], M. Bethermin[140], F. Beutler[47], M. Bonici[98,37], F. Bouchè[141,43], M. L. Brown[48], S. Bruton[13], A. Calabro[9], B. Camacho Quevedo[19,21,2], C. S. Carvalho[142], T. E. Collett[128], A. R. Cooray[143], P. Corcho-Caballero[10], B. Csizi[110], O. Cucciati[6], T. de Boer[44], G. Desprez[10], A. Díaz-Sánchez[144], S. Di Domizio[27,28], J. M. Diego[145], P.-A. Duc[140], V. Duret[146], A. Enia[121,6], Y. Fang[26], A. Farina[17,28], A. M. N. Ferguson[47], A. Finoguenov[78], A. Fontana[9], A. Franco[147,148,149], N. Frusciante[150,151], A. Fumagalli[2], K. Ganga[90], E. Gaztanaga[41,42,128], Z. Ghaffari[2,19], F. Giacomini[23], F. Gianotti[6], G. Gozaliasl[152,78], A. Gruppuso[6,23], M. Guidi[22,6], N. A. Hatch[153], C. Hernández-Monteagudo[122,46], T. Heuberger[84], J. Hjorth[154], M. Jauzac[123,87,155,156,106], S. Joudaki[39], J. J. E. Kajava[157,158,159], D. Karagiannis[160,115,161], J. Kim[64], C. C. Kirkpatrick[162], A. Kovács[139,138], I. Kovačić[136], K. Koyama[128], S. Kruk[16], M. C. Lam[47], M. Lattanzi[116], S. Lee[163,69], J. Le Graet[11], M. Lembo[88], M. D. Lepinzan[2], J. Lesgourgues[164], T. I. Liaudat[165], L. Linke[110], S. J. Liu[61], F. Mannucci[166], F. R. Marleau[110], C. J. A. P. Martins[167,32], M. Migliaccio[168,169], M. Miluzio[16,170], G. Morgante[6], K. Naidoo[128,12], P. Natoli[115,116], A. Navarro-Alsina[85], A. Nersesian[171,136], S. Nesseris[105], L. Nicastro[6], F. Oppizzi[28,60,104], F. Pace[34,35,36,56], M. J. Page[54], D. Paoletti[6,62], F. Passalacqua[60], C. Pattison[128], A. Pisani[11], L. Pizzuti[172], J. J. Popp[173], D. Potter[174], M. Poulain[175], G. W. Pratt[18], S. Quai[86,6], F. Ricci[176,9], W. Roster[25], M. Sahlén[177], D. B. Sanders[44], A. Schneider[174], D. Sciotti[9,38], E. Sellentin[178,4], S. Serjeant[173], L. C. Smith[179], I. Szapudi[44], M. Talia[86,6], G. Testera[28], R. Teyssier[180], S. Tosi[27,17,28], C. Uhlemann[181], M. Urbano[153,140], C. Valieri[23],

A. Venhola[175], D. Vergani[6], A. Viitanen[57, 162, 9], E. Vilenius[54], S. Vinciguerra[81], M. von Wietersheim-Kramsta[87, 123], N. A. Walton[179], L. Wang[182, 10], A. H. Wright[183], and D. Scott[184]

[1] Space Science Data Center, Italian Space Agency, via del Politecnico snc, 00133 Roma, Italy
[2] INAF-Osservatorio Astronomico di Trieste, Via G. B. Tiepolo 11, 34143 Trieste, Italy
[3] Caltech/IPAC, 1200 E. California Blvd., Pasadena, CA 91125, USA
[4] Leiden Observatory, Leiden University, Einsteinweg 55, 2333 CC Leiden, The Netherlands
[5] Aerospace Logistics Technology Engineering Company, Corso Marche 79, 10146 Torino, Italy
[6] INAF-Osservatorio di Astrofisica e Scienza dello Spazio di Bologna, Via Piero Gobetti 93/3, 40129 Bologna, Italy
[7] Centre de Recherche Astrophysique de Lyon, UMR5574, CNRS, Université Claude Bernard Lyon 1, ENS de Lyon, 69230, Saint-Genis-Laval, France
[8] Université Lyon 1, CNRS/IN2P3, IP2I Lyon, Villeurbanne, France
[9] INAF-Osservatorio Astronomico di Roma, Via Frascati 33, 00078 Monteporzio Catone, Italy
[10] Kapteyn Astronomical Institute, University of Groningen, PO Box 800, 9700 AV Groningen, The Netherlands
[11] Aix-Marseille Université, CNRS/IN2P3, CPPM, Marseille, France
[12] Max-Planck-Institut für Astronomie, Königstuhl 17, 69117 Heidelberg, Germany
[13] California Institute of Technology, 1200 E California Blvd, Pasadena, CA 91125, USA
[14] INAF-Osservatorio Astronomico di Padova, Via dell'Osservatorio 5, 35122 Padova, Italy
[15] Infrared Processing and Analysis Center, California Institute of Technology, Pasadena, CA 91125, USA
[16] ESAC/ESA, Camino Bajo del Castillo, s/n., Urb. Villafranca del Castillo, 28692 Villanueva de la Cañada, Madrid, Spain
[17] INAF-Osservatorio Astronomico di Brera, Via Brera 28, 20122 Milano, Italy
[18] Université Paris-Saclay, Université Paris Cité, CEA, CNRS, AIM, 91191, Gif-sur-Yvette, France
[19] IFPU, Institute for Fundamental Physics of the Universe, via Beirut 2, 34151 Trieste, Italy
[20] INFN, Sezione di Trieste, Via Valerio 2, 34127 Trieste TS, Italy
[21] SISSA, International School for Advanced Studies, Via Bonomea 265, 34136 Trieste TS, Italy
[22] Dipartimento di Fisica e Astronomia, Università di Bologna, Via Gobetti 93/2, 40129 Bologna, Italy
[23] INFN-Sezione di Bologna, Viale Berti Pichat 6/2, 40127 Bologna, Italy
[24] ATG Europe BV, Huygensstraat 34, 2201 DK Noordwijk, The Netherlands
[25] Max Planck Institute for Extraterrestrial Physics, Giessenbachstr. 1, 85748 Garching, Germany
[26] Universitäts-Sternwarte München, Fakultät für Physik, Ludwig-Maximilians-Universität München, Scheinerstr. 1, 81679 München, Germany
[27] Dipartimento di Fisica, Università di Genova, Via Dodecaneso 33, 16146, Genova, Italy
[28] INFN-Sezione di Genova, Via Dodecaneso 33, 16146, Genova, Italy
[29] Department of Physics "E. Pancini", University Federico II, Via Cinthia 6, 80126, Napoli, Italy
[30] INAF-Osservatorio Astronomico di Capodimonte, Via Moiariello 16, 80131 Napoli, Italy
[31] European Southern Observatory, Karl-Schwarzschild-Str. 2, 85748 Garching, Germany
[32] Instituto de Astrofísica e Ciências do Espaço, Universidade do Porto, CAUP, Rua das Estrelas, PT4150-762 Porto, Portugal
[33] Faculdade de Ciências da Universidade do Porto, Rua do Campo de Alegre, 4150-007 Porto, Portugal
[34] Dipartimento di Fisica, Università degli Studi di Torino, Via P. Giuria 1, 10125 Torino, Italy
[35] INFN-Sezione di Torino, Via P. Giuria 1, 10125 Torino, Italy
[36] INAF-Osservatorio Astrofisico di Torino, Via Osservatorio 20, 10025 Pino Torinese (TO), Italy
[37] INAF-IASF Milano, Via Alfonso Corti 12, 20133 Milano, Italy
[38] INFN-Sezione di Roma, Piazzale Aldo Moro, 2 - c/o Dipartimento di Fisica, Edificio G. Marconi, 00185 Roma, Italy
[39] Centro de Investigaciones Energéticas, Medioambientales y Tecnológicas (CIEMAT), Avenida Complutense 40, 28040 Madrid, Spain
[40] Port d'Informació Científica, Campus UAB, C. Albareda s/n, 08193 Bellaterra (Barcelona), Spain
[41] Institute of Space Sciences (ICE, CSIC), Campus UAB, Carrer de Can Magrans, s/n, 08193 Barcelona, Spain
[42] Institut d'Estudis Espacials de Catalunya (IEEC), Edifici RDIT, Campus UPC, 08860 Castelldefels, Barcelona, Spain
[43] INFN – Sezione di Napoli, Via Cinthia 6, 80126, Napoli, Italy
[44] Institute for Astronomy, University of Hawaii, 2680 Woodlawn Drive, Honolulu, HI 96822, USA
[45] Dipartimento di Fisica e Astronomia "Augusto Righi" - Alma Mater Studiorum Università di Bologna, Viale Berti Pichat 6/2, 40127 Bologna, Italy
[46] Instituto de Astrofísica de Canarias, E-38205 La Laguna, Tenerife, Spain
[47] Institute for Astronomy, University of Edinburgh, Royal Observatory, Blackford Hill, Edinburgh EH9 3HJ, UK
[48] Jodrell Bank Centre for Astrophysics, Department of Physics and Astronomy, University of Manchester, Oxford Road, Manchester M13 9PL, UK
[49] European Space Agency/ESRIN, Largo Galileo Galilei 1, 00044 Frascati, Roma, Italy
[50] Institut de Ciències del Cosmos (ICCUB), Universitat de Barcelona (IEEC-UB), Martí i Franquès 1, 08028 Barcelona, Spain
[51] Institució Catalana de Recerca i Estudis Avançats (ICREA), Passeig de Lluís Companys 23, 08010 Barcelona, Spain
[52] Institut de Ciencies de l'Espai (IEEC-CSIC), Campus UAB, Carrer de Can Magrans, s/n Cerdanyola del Vallés, 08193 Barcelona, Spain
[53] Université Lyon 1, CNRS/IN2P3, IUF, IP2I Lyon, Villeurbanne, France
[54] Mullard Space Science Laboratory, University College London, Holmbury St Mary, Dorking, Surrey RH5 6NT, UK
[55] Departamento de Física, Faculdade de Ciências, Universidade de Lisboa, Edifício C8, Campo Grande, PT1749-016 Lisboa, Portugal
[56] Instituto de Astrofísica e Ciências do Espaço, Faculdade de Ciências, Universidade de Lisboa, Campo Grande, 1749-016 Lisboa, Portugal
[57] Department of Astronomy, University of Geneva, ch. d'Ecogia 16, 1290 Versoix, Switzerland
[58] Université Paris-Saclay, CNRS, Institut d'astrophysique spatiale, 91405, Orsay, France
[59] Institut universitaire de France (IUF), 1 rue Descartes, 75231 PARIS CEDEX 05, France
[60] INFN-Padova, Via Marzolo 8, 35131 Padova, Italy
[61] INAF-Istituto di Astrofisica e Planetologia Spaziali, via del Fosso del Cavaliere, 100, 00100 Roma, Italy
[62] INFN-Bologna, Via Irnerio 46, 40126 Bologna, Italy
[63] School of Physics, HH Wills Physics Laboratory, University of Bristol, Tyndall Avenue, Bristol, BS8 1TL, UK

[64] Department of Physics, University of Oxford, Keble Road, Oxford OX1 3RH, UK
[65] University Observatory, LMU Faculty of Physics, Scheinerstr. 1, 81679 Munich, Germany
[66] Dipartimento di Fisica "Aldo Pontremoli", Università degli Studi di Milano, Via Celoria 16, 20133 Milano, Italy
[67] INFN-Sezione di Milano, Via Celoria 16, 20133 Milano, Italy
[68] Institute of Theoretical Astrophysics, University of Oslo, P.O. Box 1029 Blindern, 0315 Oslo, Norway
[69] Jet Propulsion Laboratory, California Institute of Technology, 4800 Oak Grove Drive, Pasadena, CA, 91109, USA
[70] School of Physics and Astronomy, Lancaster University, Lancaster, LA1 4YB, UK
[71] Felix Hormuth Engineering, Goethestr. 17, 69181 Leimen, Germany
[72] Technical University of Denmark, Elektrovej 327, 2800 Kgs. Lyngby, Denmark
[73] Cosmic Dawn Center (DAWN), Denmark
[74] Université PSL, Observatoire de Paris, Sorbonne Université, CNRS, LERMA, 75014, Paris, France
[75] Université Paris-Cité, 5 Rue Thomas Mann, 75013, Paris, France
[76] NASA Goddard Space Flight Center, Greenbelt, MD 20771, USA
[77] Université de Genève, Département de Physique Théorique and Centre for Astroparticle Physics, 24 quai Ernest-Ansermet, CH-1211 Genève 4, Switzerland
[78] Department of Physics, P.O. Box 64, University of Helsinki, 00014 Helsinki, Finland
[79] Helsinki Institute of Physics, Gustaf Hällströmin katu 2, University of Helsinki, 00014 Helsinki, Finland
[80] Laboratoire d'etude de l'Univers et des phenomenes eXtremes, Observatoire de Paris, Université PSL, Sorbonne Université, CNRS, 92190 Meudon, France
[81] Aix-Marseille Université, CNRS, CNES, LAM, Marseille, France
[82] SKAO, Jodrell Bank, Lower Withington, Macclesfield SK11 9FT, UK
[83] Centre de Calcul de l'IN2P3/CNRS, 21 avenue Pierre de Coubertin 69627 Villeurbanne Cedex, France
[84] University of Applied Sciences and Arts of Northwestern Switzerland, School of Computer Science, 5210 Windisch, Switzerland
[85] Universität Bonn, Argelander-Institut für Astronomie, Auf dem Hügel 71, 53121 Bonn, Germany
[86] Dipartimento di Fisica e Astronomia "Augusto Righi" - Alma Mater Studiorum Università di Bologna, via Piero Gobetti 93/2, 40129 Bologna, Italy
[87] Department of Physics, Institute for Computational Cosmology, Durham University, South Road, Durham, DH1 3LE, UK
[88] Institut d'Astrophysique de Paris, UMR 7095, CNRS, and Sorbonne Université, 98 bis boulevard Arago, 75014 Paris, France
[89] Niels Bohr Institute, University of Copenhagen, Jagtvej 128, 2200 Copenhagen, Denmark
[90] Université Paris Cité, CNRS, Astroparticule et Cosmologie, 75013 Paris, France
[91] CNRS-UCB International Research Laboratory, Centre Pierre Binétruy, IRL2007, CPB-IN2P3, Berkeley, USA
[92] Institute of Physics, Laboratory of Astrophysics, Ecole Polytechnique Fédérale de Lausanne (EPFL), Observatoire de Sauverny, 1290 Versoix, Switzerland
[93] Dipartimento di Fisica - Sezione di Astronomia, Università di Trieste, Via Tiepolo 11, 34131 Trieste, Italy
[94] Telespazio UK S.L. for European Space Agency (ESA), Camino bajo del Castillo, s/n, Urbanizacion Villafranca del Castillo, Villanueva de la Cañada, 28692 Madrid, Spain
[95] Institut de Física d'Altes Energies (IFAE), The Barcelona Institute of Science and Technology, Campus UAB, 08193 Bellaterra (Barcelona), Spain
[96] School of Mathematics and Physics, University of Surrey, Guildford, Surrey, GU2 7XH, UK
[97] European Space Agency/ESTEC, Keplerlaan 1, 2201 AZ Noordwijk, The Netherlands
[98] Waterloo Centre for Astrophysics, University of Waterloo, Waterloo, Ontario N2L 3G1, Canada
[99] Department of Physics and Astronomy, University of Waterloo, Waterloo, Ontario N2L 3G1, Canada
[100] Perimeter Institute for Theoretical Physics, Waterloo, Ontario N2L 2Y5, Canada
[101] Centre National d'Etudes Spatiales – Centre spatial de Toulouse, 18 avenue Edouard Belin, 31401 Toulouse Cedex 9, France
[102] Institute of Space Science, Str. Atomistilor, nr. 409 Măgurele, Ilfov, 077125, Romania
[103] Institute for Particle Physics and Astrophysics, Dept. of Physics, ETH Zurich, Wolfgang-Pauli-Strasse 27, 8093 Zurich, Switzerland
[104] Dipartimento di Fisica e Astronomia "G. Galilei", Università di Padova, Via Marzolo 8, 35131 Padova, Italy
[105] Instituto de Física Teórica UAM-CSIC, Campus de Cantoblanco, 28049 Madrid, Spain
[106] Institut de Recherche en Astrophysique et Planétologie (IRAP), Université de Toulouse, CNRS, UPS, CNES, 14 Av. Edouard Belin, 31400 Toulouse, France
[107] Université St Joseph; Faculty of Sciences, Beirut, Lebanon
[108] Departamento de Física, FCFM, Universidad de Chile, Blanco Encalada 2008, Santiago, Chile
[109] Université Côte d'Azur, Observatoire de la Côte d'Azur, CNRS, Laboratoire Lagrange, Bd de l'Observatoire, CS 34229, 06304 Nice cedex 4, France
[110] Universität Innsbruck, Institut für Astro- und Teilchenphysik, Technikerstr. 25/8, 6020 Innsbruck, Austria
[111] Cosmic Dawn Center (DAWN)
[112] Universidad Politécnica de Cartagena, Departamento de Electrónica y Tecnología de Computadoras, Plaza del Hospital 1, 30202 Cartagena, Spain
[113] European University of Technology EUt+, European Union
[114] Centre for Information Technology, University of Groningen, P.O. Box 11044, 9700 CA Groningen, The Netherlands
[115] Dipartimento di Fisica e Scienze della Terra, Università degli Studi di Ferrara, Via Giuseppe Saragat 1, 44122 Ferrara, Italy
[116] Istituto Nazionale di Fisica Nucleare, Sezione di Ferrara, Via Giuseppe Saragat 1, 44122 Ferrara, Italy
[117] ICSC - Centro Nazionale di Ricerca in High Performance Computing, Big Data e Quantum Computing, Via Magnanelli 2, Bologna, Italy
[118] INAF, Istituto di Radioastronomia, Via Piero Gobetti 101, 40129 Bologna, Italy
[119] Astronomical Observatory of the Autonomous Region of the Aosta Valley (OAVdA), Loc. Lignan 39, I-11020, Nus (Aosta Valley), Italy
[120] Department of Mathematical Physics, Institute of Physics, University of São Paulo, R. do Matão 1371, 05508-090, São Paulo, SP, Brazil
[121] CEA Saclay, DFR/IRFU, Service d'Astrophysique, Bat. 709, 91191 Gif-sur-Yvette, France
[122] Universidad de La Laguna, Dpto. Astrofísica, E-38206 La Laguna, Tenerife, Spain
[123] Department of Physics, Centre for Extragalactic Astronomy, Durham University, South Road, Durham, DH1 3LE, UK
[124] Oskar Klein Centre for Cosmoparticle Physics, Department of Physics, Stockholm University, Stockholm, SE-106 91, Sweden

[125] Astrophysics Group, Blackett Laboratory, Imperial College London, London SW7 2AZ, UK
[126] Univ. Grenoble Alpes, CNRS, Grenoble INP, LPSC-IN2P3, 53, Avenue des Martyrs, 38000 Grenoble, France
[127] Dipartimento di Fisica, Sapienza Università di Roma, Piazzale Aldo Moro 2, 00185 Roma, Italy
[128] Institute of Cosmology and Gravitation, University of Portsmouth, Portsmouth PO1 3FX, UK
[129] Institut d'Astrophysique de Paris, 98bis Boulevard Arago, 75014, Paris, France
[130] ICL, Junia, Université Catholique de Lille, LITL, 59000 Lille, France
[131] Center for Astrophysics and Cosmology, University of Nova Gorica, Nova Gorica, Slovenia
[132] Department of Astronomy, Indiana University, 727 East Third Street, Bloomington, IN 47405, USA
[133] CERCA/ISO, Department of Physics, Case Western Reserve University, 10900 Euclid Avenue, Cleveland, OH 44106, USA
[134] Laboratoire Univers et Théorie, Observatoire de Paris, Université PSL, Université Paris Cité, CNRS, 92190 Meudon, France
[135] Departamento de Física Fundamental. Universidad de Salamanca. Plaza de la Merced s/n. 37008 Salamanca, Spain
[136] Universiteit Gent, Department of Physics and Astronomy, Proeftuinstraat 86 N3, 9000 Ghent, Belgium
[137] Aix-Marseille Université, Université de Toulon, CNRS, CPT, Marseille, France
[138] Konkoly Observatory, HUN-REN CSFK, MTA Centre of Excellence, Budapest, Konkoly Thege Miklós út 15-17. H-1121, Hungary
[139] MTA-CSFK Lendület Large-Scale Structure Research Group, Konkoly-Thege Miklós út 15-17, H-1121 Budapest, Hungary
[140] Université de Strasbourg, CNRS, Observatoire astronomique de Strasbourg, UMR 7550, 67000 Strasbourg, France
[141] Scuola Superiore Meridionale, Via Mezzocannone 4, 80138, Napoli, Italy
[142] Instituto de Astrofísica e Ciências do Espaço, Faculdade de Ciências, Universidade de Lisboa, Tapada da Ajuda, 1349-018 Lisboa, Portugal
[143] Department of Physics & Astronomy, University of California Irvine, Irvine CA 92697, USA
[144] Departamento Física Aplicada, Universidad Politécnica de Cartagena, Campus Muralla del Mar, 30202 Cartagena, Murcia, Spain
[145] Instituto de Física de Cantabria, Edificio Juan Jordá, Avenida de los Castros, 39005 Santander, Spain
[146] Univ. Grenoble Alpes, CNRS, IPAG, 38000 Grenoble, France
[147] Department of Mathematics and Physics E. De Giorgi, University of Salento, Via per Arnesano, CP-I93, 73100, Lecce, Italy
[148] INFN, Sezione di Lecce, Via per Arnesano, CP-193, 73100, Lecce, Italy
[149] INAF-Sezione di Lecce, c/o Dipartimento Matematica e Fisica, Via per Arnesano, 73100, Lecce, Italy
[150] Dipartimento di Fisica "E. Pancini", Universita degli Studi di Napoli Federico II, Via Cinthia 6, 80126, Napoli, Italy
[151] INFN Sezione di Napoli, Universita degli Studi di Napoli "Federico II", Compl. Univ. di Monte S. Angelo, Edificio G, Via Cinthia, I-80126, Napoli, Italy
[152] Department of Computer Science, Aalto University, PO Box 15400, Espoo, FI-00 076, Finland
[153] School of Physics and Astronomy, University of Nottingham, University Park, Nottingham NG7 2RD, UK
[154] DARK, Niels Bohr Institute, University of Copenhagen, Jagtvej 155, 2200 Copenhagen, Denmark
[155] Astrophysics Research Centre, University of KwaZulu-Natal, Westville Campus, Durban 4041, South Africa
[156] School of Mathematics, Statistics & Computer Science, University of KwaZulu-Natal, Westville Campus, Durban 4041, South Africa
[157] Department of Physics and Astronomy, Vesilinnantie 5, University of Turku, 20014 Turku, Finland
[158] Finnish Centre for Astronomy with ESO (FINCA), Quantum, Vesilinnantie 5, University of Turku, 20014 Turku, Finland
[159] Serco for European Space Agency (ESA), Camino bajo del Castillo, s/n, Urbanizacion Villafranca del Castillo, Villanueva de la Cañada, 28692 Madrid, Spain
[160] Van Swinderen Institute, University of Groningen, Nijenborgh 3, 9747 AG Groningen, The Netherlands
[161] Department of Physics and Astronomy, University of the Western Cape, Bellville, Cape Town, 7535, South Africa
[162] Department of Physics and Helsinki Institute of Physics, Gustaf Hällströmin katu 2, University of Helsinki, 00014 Helsinki, Finland
[163] Ohio University, Physics & Astronomy Department,1 Ohio University, Athens, OH 45701, USA
[164] Institute for Theoretical Particle Physics and Cosmology (TTK), RWTH Aachen University, 52056 Aachen, Germany
[165] IRFU, CEA, Université Paris-Saclay 91191 Gif-sur-Yvette Cedex, France
[166] INAF-Osservatorio Astrofisico di Arcetri, Largo E. Fermi 5, 50125, Firenze, Italy
[167] Centro de Astrofísica da Universidade do Porto, Rua das Estrelas, 4150-762 Porto, Portugal
[168] Dipartimento di Fisica, Università di Roma Tor Vergata, Via della Ricerca Scientifica 1, Roma, Italy
[169] INFN, Sezione di Roma 2, Via della Ricerca Scientifica 1, Roma, Italy
[170] HE Space for European Space Agency (ESA), Camino bajo del Castillo, s/n, Urbanizacion Villafranca del Castillo, Villanueva de la Cañada, 28692 Madrid, Spain
[171] STAR Institute, University of Liège, Quartier Agora, Allée du six Août 19c, 4000 Liège, Belgium
[172] Dipartimento di Fisica "G. Occhialini", Università degli Studi di Milano Bicocca, Piazza della Scienza 3, 20126 Milano, Italy
[173] School of Physical Sciences, The Open University, Milton Keynes, MK7 6AA, UK
[174] Department of Astrophysics, University of Zurich, Winterthurerstrasse 190, 8057 Zurich, Switzerland
[175] Space physics and astronomy research unit, University of Oulu, Pentti Kaiteran katu 1, FI-90014 Oulu, Finland
[176] Department of Mathematics and Physics, Roma Tre University, Via della Vasca Navale 84, 00146 Rome, Italy
[177] Theoretical astrophysics, Department of Physics and Astronomy, Uppsala University, Box 524, 751 20 Uppsala, Sweden
[178] Mathematical Institute, University of Leiden, Einsteinweg 55, 2333 CA Leiden, The Netherlands
[179] Institute of Astronomy, University of Cambridge, Madingley Road, Cambridge CB3 0HA, UK
[180] Department of Astrophysical Sciences, Peyton Hall, Princeton University, Princeton, NJ 08544, USA
[181] Fakultät für Physik, Universität Bielefeld, Postfach 100131, 33501 Bielefeld, Germany
[182] SRON Netherlands Institute for Space Research, Landleven 12, 9747 AD, Groningen, The Netherlands
[183] Ruhr University Bochum, Faculty of Physics and Astronomy, Astronomical Institute (AIRUB), German Centre for Cosmological Lensing (GCCL), 44780 Bochum, Germany
[184] Department of Physics and Astronomy, University of British Columbia, Vancouver, BC V6T 1Z1, Canada

⋆ e-mail: gianluca.polenta@asi.it

Appendix A: Statistics for the non-transient BPM

Table A.1. NISP detector non-transient DQ flags in DR1.

DetID[a]	Invalid pixels[b]						Informational[b]	
	DISCONN	ZEROQE	SUPERQE	BADBASE	SAT	FLOWER	LOWQE	HOT
11	450	747	290	27	15	3926	591	3601
12	3655	5399	7038	25	1	15582	953	10756
13	936	1261	551	74	54	6360	219	3661
14	849	1858	579	183	155	22047	597	12830
21	728	1275	16	171	115	7423	292	4714
22	2971	3510	1313	2127	92	9881	331	8029
23	1811	1992	2373	75	51	7105	605	3961
24	490	698	302	15	10	4270	216	2160
31	1721	2054	992	72	36	6870	725	7747
32	3399	895	307	76	128	25274	420	5816
33	768	1288	644	95	89	7837	402	7671
34	1388	2072	249	105	11	6113	390	5764
41	3220	1858	339	63	17	18604	584	2818
42	663	847	404	62	4800	143	390	4086
43	955	1129	401	17	3	2672	278	1997
44	6016	7420	558	707	33	5588	1542	11652

Notes. [(a)] Detector slot position in the NISP FPA; see figure A.1 in Euclid Collaboration: Jahnke et al. (2025). [(b)] Pixel flag column names correspond to metadata keywords in the DQ layer within each data product.

The statistics of the non-transient DQ flags identified for the NISP detectors in DR1 are reported in Table A.1.

Appendix B: Additional validation of the small-scale flat-field stability

B.1. Masks, temporal sampling, and statistical checks

The monitoring sequence in Sect. 3.2.1 contains one $H_{\rm E}$ master flat per month from March 2024 to April 2026, except for November 2024 and November 2025, for which no product is available. Temporal separations are calculated from the observing dates; the missing months are not interpolated.

For each detector, the common temporal mask retains pixels that are finite, positive, have zero data-quality (DQ) value, and lie outside the vignetting mask at every epoch. We dilate the excluded regions by 3 pixels before constructing the small-scale maps. The zero-DQ requirement excludes all flagged pixels, including informational flags, and is therefore stricter than excluding only the `INVALID` bit described in Sect. 3.1.1. The retained fraction has a median of 96.25% across detectors and a range of 90.62–98.81%. These measurements describe the pixels retained at every epoch; they do not measure changes in the population of newly flagged pixels.

In the numerical calculation, we divide each master flat by its median over the common mask before smoothing. The mask-aware Gaussian operator smooths the valid-pixel-weighted image and the validity weights separately and divides the two results. Because the mask is fixed, the detector-median normalisation cancels in the ratio that defines S_d. Equation (3) is therefore equivalent to the implemented calculation.

The reference-relative residual is $\Delta \ln S_{d,\mathrm{early}}(\mathbf{x}, t) = \ln[S_d(\mathbf{x}, t)/S_{d,\mathrm{early}}(\mathbf{x})]$. The first three epochs enter $S_{d,\mathrm{early}}$ and are not independent of it. Their residuals are retained in the diagnostic heatmap but omitted from the reference-relative time-series plot. The adjacent-epoch statistic uses consecutive available products, including the longer intervals across the missing months. The late-to-early comparison uses two disjoint three-epoch median stacks.

The structure function uses all 276 distinct epoch pairs, with 42, 53, 90, 65, and 26 pairs in the lag bins 0–90, 90–180, 180–365, 365–550, and 550–800 days, respectively. Each pair contributes one measurement per detector. Pairs sharing an epoch are not independent. For the jackknife calculation, we omit each epoch in turn, remove every pair containing that epoch, and recalculate the lag-bin medians. The resulting jackknife standard errors describe sensitivity to the sampled epochs, not the unknown contributions of the calibration source or processing.

Detector medians and pooled focal-plane statistics are calculated separately. For example, the range 0.246–0.291% describes the 16 detector-level late-to-early scatters, whereas 0.264% is calculated from the pooled pixel distribution. The latter distribution also supplies the percentile annotations in Fig. B.1; its median residual is 0.009%.

The main residual mosaic and its statistics use the same common mask, with no additional edge exclusion. As a separate check, excluding the outer 64 pixels of each detector changes the pooled late-to-early σ_{68} from 0.2640% to 0.2620%, a relative difference of 0.76%. Thus, these edge regions do not dominate the pooled scatter. Changing the Gaussian standard deviation for the smoothing from 64 to 32 or 128 pixels changes the final reference-relative scatter by less than 1% relative to the nominal result. The morphology of narrow boundary haloes remains scale dependent, so the stability of the global statistic does not establish the origin of individual boundary structures.

B.2. Measurements of residual structures

All measurements in this section use the late-to-early logarithmic residual on the native detector grid, before the display rotations and 8×8 binning in Fig. B.1. Positive and negative components are identified separately. A local contrast is the median residual within a selected region minus the median residual in its surrounding control region. These contrasts describe struc-

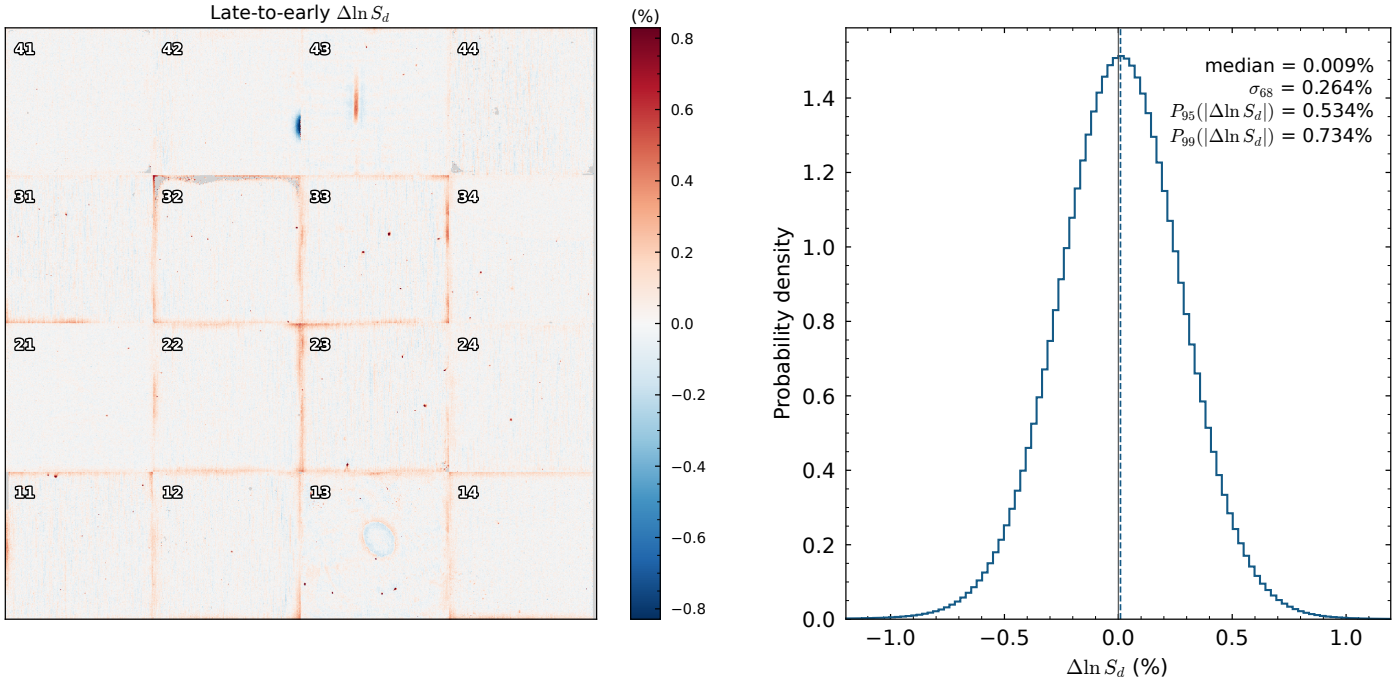


Fig. B.1. Late-to-early small-scale logarithmic residual, comparing pixel-wise median stacks of the final three and first three epochs. *Left:* The focal-plane mosaic, binned 8×8 for display only. The colour scale is symmetric about zero, detector residual medians are retained, and pixels excluded by the common temporal mask are shown in neutral grey. No additional detector-edge exclusion is applied. *Right:* distribution and annotated statistics of all unbinned valid focal-plane pixels.

tures in the delivered master flats and are not assigned a physical origin.

Detector boundaries and extended features. For each of the four edges of each detector, we form a profile of the median residual as a function of distance from the edge. We compare the median of this profile over distances 0–7 pixels with its median over an interior control interval of 32–63 pixels, with both intervals chosen according to the adopted binning and Gaussian smoothing scales. A positive edge excess is selected when the difference exceeds both 0.05% and three times the σ_{68} of the control-profile values. This criterion selects 27 of the 64 edges, distributed over ten detectors. Among these selected edges, the median edge-minus-control contrast is 0.087%, with 16th–84th percentiles of 0.066–0.114%. These are empirical profile-selection thresholds, not false-alarm probabilities.

The negative feature on detector 42 intersects a detector edge. Its selected footprint spans 74×291 native pixels and has a median local contrast of −0.499%. The dimensions describe the observed, edge-truncated footprint, not the full extent of the feature. Detector 43 contains a vertical positive band, and detector 13 contains a broad negative ellipse with a positive surround (see Fig. B.1). Given the amplitude of the detected features and the small fraction of pixels involved across the three regions, their impact on the overall quality of the NIR images is negligible. In terms of their local impact, the measured contrasts are well within the 1.5% relative calibration accuracy requirement.

Compact positive regions. We construct a detection map by subtracting the late-to-early residual smoothed with a Gaussian of $\sigma = 12$ pixels from the same residual smoothed with $\sigma = 1.5$ pixels. Both convolutions are normalised by their valid-pixel support. For each detector, we estimate the median and a robust scale from control pixels at least 24 pixels from detector edges and 8 pixels from invalid regions. The scale is the median absolute deviation multiplied by 1.4826, with iterative clipping at 4.5 times that scale. This detection scale differs from the σ_{68} used for the stability measurements. It includes correlated residual structure and is not a measurement of master-flat noise.

We identify connected positive regions above the control median by at least 2.5 times the detection scale, retaining regions that contain a pixel at least 5 times that scale above the median. Connectivity includes the eight neighbouring pixels. The compact-region selection requires at least nine valid pixels, a second-moment ellipse axis ratio no greater than 3, and a minor-axis length of at least 1 pixel. Regions with a major-axis or bounding-box extent of 80 pixels or more are classified separately as elongated structures. We exclude footprints that touch a detector edge or invalid pixel, overlap the targeted positive surround on detector 13, or lie within 2 pixels of an opposite-sign component with an unsmoothed negative residual below −0.25%. These feature-selection restrictions do not alter the common mask used for the global stability measurements or the main mosaic.

For a selected footprint with area A in native-pixel units, we define the area-equivalent diameter as

$$D_{\rm eq} = 2\sqrt{A/\pi}\,. \tag{B.1}$$

We measure the local contrast on the original, unsmoothed residual using the selected footprint and a surrounding control annulus formed by binary dilations of 5 and 18 pixels. Invalid pixels and other detected components are excluded from the control annulus. Detection smoothing therefore determines the footprint, but not the residual values used to measure its contrast.

The nominal selection contains 639 compact positive regions across all 16 detectors. Their area-equivalent diameters have a median of 5.4 pixels, with 16th–84th percentiles of 4.2–7.6 pix-

els. Their local contrasts have a median of 0.22%, with 16th–84th percentiles of 0.09–0.33%. These intervals describe the selected population, not uncertainties on its medians. The diameters describe thresholded footprints and depend on the detection smoothing and selection thresholds; they are not intrinsic detector-defect sizes. Most selected regions are smaller than the 8-pixel display bins in Fig. B.1; their sizes are measured from the native arrays, not from that mosaic.

B.3. Detector-wide changes in master-flat normalisation

We measure detector-wide changes separately from the small-scale residuals. Let $\mathcal{F}_{d,\mathrm{early}}(\mathbf{x})$ be the pixel-wise median of the first three master flats before detector-median normalisation. We define

$$m_d(t) = \mathrm{median}_{\mathbf{x}\in\Omega_d} \ln\left[\frac{\mathcal{F}_d(\mathbf{x},t)}{\mathcal{F}_{d,\mathrm{early}}(\mathbf{x})}\right]. \tag{B.2}$$

At the final epoch, the median of $100\,m_d(t)$ across detectors is −0.008%, with a range from −0.100% on detector 33 to +0.039% on detector 22 (Fig. B.2). These quantities describe detector-wide scale changes in the delivered master flats, not an isolated measurement of detector sensitivity. A purely multiplicative detector-wide change cancels in Eq. (3) and is therefore absent from the small-scale metric.

Figure B.3 shows both the reference-relative small-scale scatter and the detector-wide scale change for each detector and epoch. The low reference-relative scatters in the first three columns result from including those epochs in the reference stack. They must not be interpreted as evidence for a transition at the fourth epoch. The blank columns mark the two months without a master-flat product.

Appendix C: Description of NIR DPs

All DPs, defined in the Euclid Common Data Model as XML files, include two main metadata elements: `DataStorage`, which provides information on the associated MEF file, and `QualityParams`, which contains statistics extracted from the MEF file to assess the quality of the DP and validate its production.

C.1. Calibrated single-epoch exposures

The `DpdNirCalibratedFrame` provides fully astrometrically and photometrically calibrated individual exposures; its structure is described in NIRQ1. In DR1, the DP structure has been extended with the new `PsfSingleStorage` element, in addition to the `DataStorage`, `BackgroundStorage`, and `PsfStorage` elements already present in Q1:

- `DataStorage` – references the MEF file containing the calibrated image data;
- `BackgroundStorage` – references the MEF file containing the background measured as described in Sect. 3.2.2;
- `PsfStorage` – references two FITS files, one containing the PSF model and one containing the PSF image, obtained from observations of the self-calibration field as described in Sect. 3.2.3 and Euclid Collaboration: da Silva et al. (2026);
- `PsfSingleStorage` – references the PSF model and image derived from the calibrated image itself.

C.2. Calibrated single-epoch catalogues

The `DpdNirCalibratedFrameCatalog` is the source catalogue extracted from the calibrated single-epoch exposure (Sect. 3.2.5). Its global metadata structure therefore mirrors that of the `DpdNirCalibratedFrame`.

The MEF file is structured into 17 header data units (HDUs): a primary HDU and 16 detector-specific HDUs, each containing a catalogue table with a wide range of parameters for the detected sources, including fluxes and magnitudes estimated from multi-aperture photometry, PSF fitting, and `SourceExtractor` `MAG_AUTO`. It is important to note that aperture corrections are not applied at this stage. While magnitudes are provided in the AB system, fluxes are still reported in units of e^-.

C.3. Stacked exposures

The `DpdNirStackedFrame` is the result of the resampling and stacking process described in Sect. 3.3, combining 4 (76) single-epoch images for EWS (self-calibration field) observations. Its MEF file consists of a single `SCI` HDU covering the entire stacked science image, together with the corresponding `RMS` and Data Quality `DQ` extensions. Further details on the resampling and stacking process are provided in Sect. 3.3.

The DP metadata elements collect all information describing the stacked observation, including the `Filter`, the `WCS` keywords used to locate the image on the sky, the `ZeroPoint` containing the effective photometric image zero point, and the `DateRange` indicating the time interval covered by the observations contributing to the stacked image.

The MEF files are referenced by the same `DataStorage`, `PsfStorage`, and `PsfSingleStorage` elements used for the single-epoch images. The `BackgroundStorage` element is not present, since the background is subtracted from the images during the stacking process (see Sect. 3.3). All photometric calibration factors are applied during the process, and therefore the stacked image is in units of μJy.

As for the calibrated single-epoch frame, the `QualityParams` metadata element contains a set of statistics for the three MEF files described above. In this case, however, the internal structure is simpler than that of the single-epoch image, since it contains a single layer corresponding to the entire focal plane.

C.4. Catalogues from NIR stacks

The catalogue extracted from the stacked image is stored in the `DpdNirStackedFrameCatalog` DP. Its metadata structure is similar to that of the stacked image, with the `DataStorage` element referencing a MEF file structured into two HDUs: a primary HDU and a second HDU containing a catalogue table with the parameters of all detected sources in the stacked image.

As for the single-epoch catalogue, aperture correction is not applied to either fluxes or magnitudes. Magnitudes are provided in the AB system, while fluxes are reported in μJy.

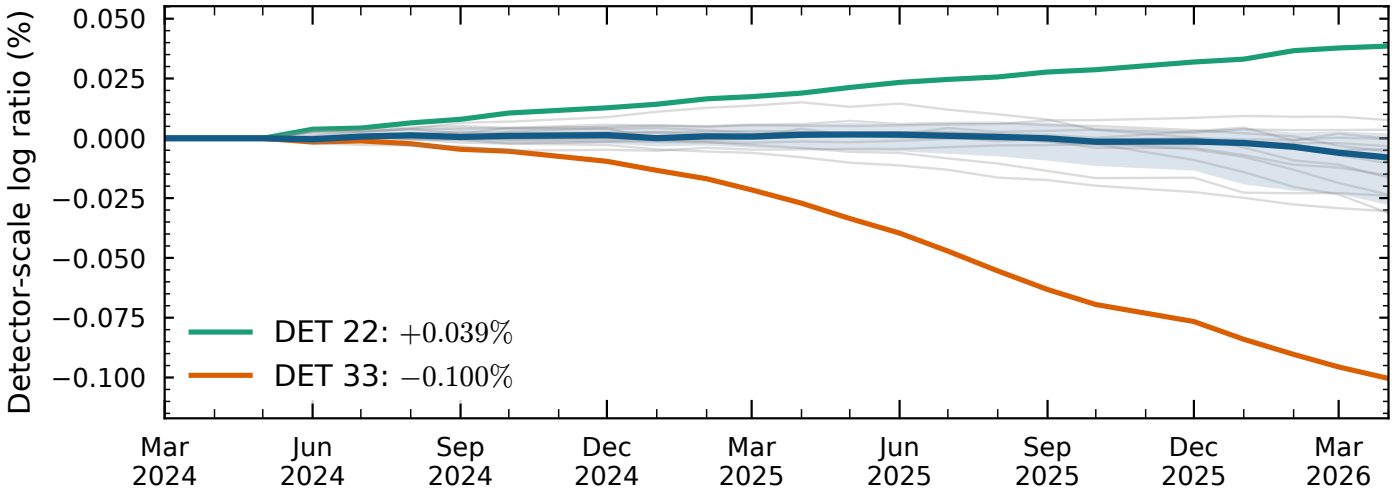


Fig. B.2. Detector-wide logarithmic changes in the master flats before median normalisation. Thin grey curves show individual detectors, while the blue curve and shaded band show the median and 16th–84th percentiles across detectors. Detectors 33 and 22 have the largest negative and positive changes at the final epoch and are highlighted. The ordinate is $100\,m_d(t)$ in percent, with $m_d(t)$ defined in Eq. (B.2). A detector-wide multiplicative change cancels from the small-scale metric.

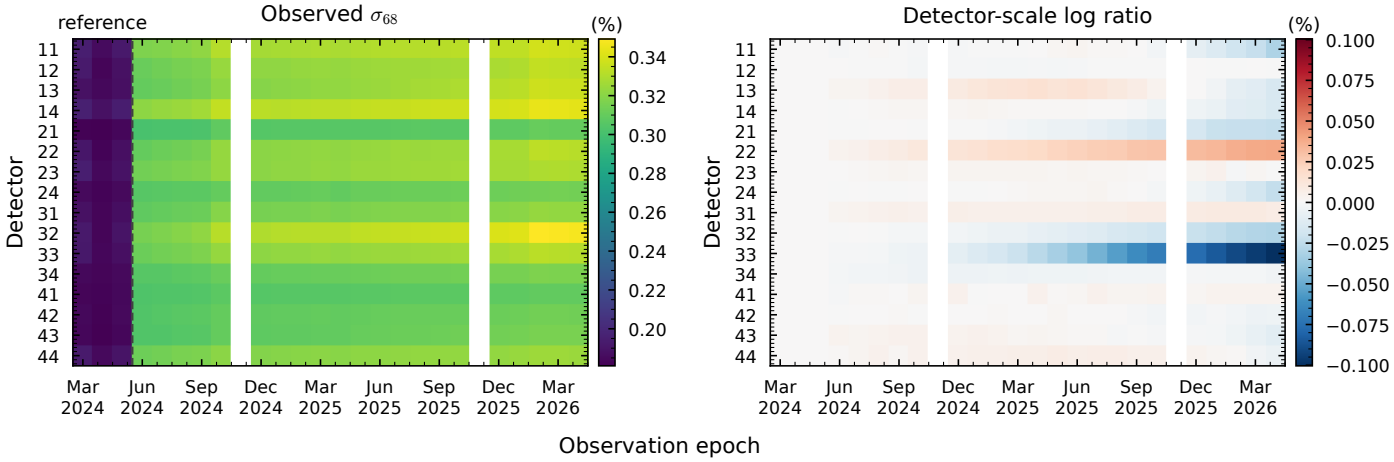


Fig. B.3. Detector-by-epoch diagnostics, with epochs in chronological order and detectors ordered by identifier. *Left:* Reference-relative scatter $\sigma_{68}(\Delta \ln S_{d,\mathrm{early}})$. The dashed line marks the end of the first-three-epoch reference interval. Residuals within that interval share data with the reference and are not comparable to those of subsequent epochs. *Right:* Detector-wide logarithmic change, $100\,m_d(t)$. Both panels are in percentages and have separate colour scales. Blank columns mark November 2024 and November 2025, for which no product is available.